Fracture and healing of elastomers: A phase-transition theory and numerical implementation

Aditya Kumar[a], Gilles A. Francfort[b,c], Oscar Lopez-Pamies[a]

[a]*Department of Civil and Environmental Engineering, University of Illinois, Urbana–Champaign, IL 61801, USA*
[b]*Courant Institute of Mathematical Sciences, 251 Mercer Street, New York, NY 10012, USA*
[c]*LAGA, Université Paris-Nord, Avenue J.-B. Clément 93430 – Villetaneuse, France*

Abstract

A macroscopic theory is proposed to describe, explain, and predict the nucleation and propagation of fracture and healing in elastomers undergoing arbitrarily large quasistatic deformations. The theory, which can be viewed as a natural generalization of the phase-field approximation of the variational theory of brittle fracture of Francfort and Marigo (1998) to account for physical attributes innate to elastomers that have been recently unveiled by experiments at high spatio-temporal resolution, rests on two central ideas. The first one is to view elastomers as solids capable to undergo finite elastic deformations and capable also to phase transition to another solid of vanishingly small stiffness: the forward phase transition serves to model the nucleation and propagation of fracture while the reverse phase transition models the possible healing. The second central idea is to take the phase transition to be driven by the competition between a combination of strain energy and hydrostatic stress concentration in the *bulk* and surface energy on the created/healed new *surfaces* in the elastomer.

From an applications point of view, the proposed theory amounts to solving a system of two coupled and nonlinear PDEs for the deformation field and an order parameter, or phase field. A numerical scheme is presented to generate solutions for these PDEs in $N = 2$ and 3 space dimensions. This is based on an efficient non-conforming finite-element discretization, which remains stable for arbitrarily large deformations and elastomers of any compressibility, together with an implicit gradient flow solver, which is able to deal with the large changes in the deformation field that can ensue locally in space and time from the nucleation of fracture. The last part of this paper is devoted to presenting sample simulations of the so-called Gent-Park experiment. Those are confronted with recent experimental results for various types of silicone elastomers.

Key words: cavitation, self-healing polymers, finite deformations, non-conforming finite elements

1. Introduction

The vast mechanics literature on the phenomenon of fracture in elastomers can be roughly classified into two categories: the literature that has focused on the *nucleation* of cavities/cracks, a phenomenon popularly referred to as cavitation, and the one that has focused on the *propagation* of existing cracks. Following in the footsteps of Gent and Lindley (1959) and Ball (1982), the former has overwhelmingly operated under the premise that cavitation in elastomers is fundamentally an elastic phenomenon. On the other hand, following the doctrine pioneered by Griffith (1921) and transcribed for finite elasticity by Rivlin and Thomas (1953), the latter has been based on the view that the propagation of cracks in elastomers is

governed by the competition between the elastic energy stored in the bulk and the surface energy dissipated through the creation of new surfaces. By and large, these two efforts on nucleation and propagation of fracture in elastomers have been pursued disconnected from one another.

In a different direction, an increasing number of papers have been recently devoted to the investigation of crack *healing* in elastomers featuring sophisticated chemistries that promote healing; see, e.g., Cordier et al. (2008), Blaiszik et al. (2010), and Bahrt Madsen et al. (2016). In spite of the fact that healing can be naturally thought of as the reverse phenomenon to fracture, there has been no recognition of this intimate connection as investigations on healing have continued to be pursued disconnected from the above two thrusts on fracture.

As part of a recent effort to understand nucleation and propagation of fracture from a unifying point of view, the analysis in Lefèvre et al. (2015) of the classical experiments of Gent and Lindley (1959) and Gent and Park (1984) and the companion analysis in Poulain et al. (2017) of analogous new experiments at higher spatio-temporal resolution (of 1 μm in space and 66.7 ms in time) have provided a thorough qualitative picture of the nucleation and ensuing growth and interaction of internal cavities/cracks in elastomers subject to externally applied quasistatic mechanical loads. *Inter alia*, this qualitative picture has established that the phenomenon of cavitation — that is, again, the nucleation of internal cavities/cracks — is fundamentally a by-product of fracture and *not* solely of elasticity as popularly thought. Remarkably, the experiments in Poulain et al. (2017), together with a more complete set of experiments by Ravi-Chandar (2016), have also revealed that internally nucleated cracks in conventional elastomers — without sophisticated chemistries — can completely heal, even when they have grown to be tens of microns in length scale, in a time scale of seconds. In a nutshell, according to the above works, the following three distinguishing features come to the fore for a given specimen along an arbitrary loading path:

- The onset of cavitation occurs via the growth by fracture[1] of sub-micron defects into cavities/cracks of micron size in regions of the elastomer that are sufficiently far away from constraints that may impede their large deformation and, more significantly, in regions where the ratio of hydrostatic stress to shear stresses is sufficiently high (e.g., near reinforcing fillers in filled elastomers). One or several cavities/cracks may nucleate at unison or in a cascade, this depending on the specifics of the specimen and of the applied loading conditions;

- Upon further loading, the nucleated cavities/cracks proceed to grow by fracture into cracks of tens of microns in size — which we term micro-cracks — and thus become visible optically. They do so, however, at a markedly lower rate than that observed during their nucleation; and

- Upon further loading, one, or several among the various micro-cracks grows by fracture into a crack of hundreds of microns in size — which we label macro-cracks — while the other micro-cracks stop growing, then decrease in size, and eventually completely heal[2]. Remarkably, the regions of the elastomer that experience healing appear to acquire different fracture and healing properties from those of the original elastomer hinting at an evolution of the underlying molecular rearrangement and/or chemical bonding due to the healing process.

In this paper, we strive to lend a modicum of theoretical credence to the above outlined phenomena by constructing a macroscopic field theory aimed at describing, explaining, and predicting the nucleation and propagation of fracture and healing in elastomers undergoing finite deformations in response to arbitrary quasistatic mechanical loads.

The theory rests on two central ideas. First view elastomers as solids that undergo finite elastic deformations and may transition to another solid of vanishingly small stiffness. The forward phase transition models

---

[1]We remind the reader that the molecular mechanisms that lead to fracture (i.e., the creation of internal new surfaces) in elastomers remain currently unclear. In particular, it is still not known the extent to which fracture is due to the geometric rearrangement of the underlying macromolecules and/or to the breaking of chemical bonds.

[2]More so than those that lead to fracture, the molecular mechanisms that lead to healing in elastomers remain currently unclear.

the nucleation and propagation of fracture while there is a possibility of a reverse phase transition that would model healing. Then take the phase transition as driven by the competition between a combination of strain energy and hydrostatic stress concentration in the *bulk* and surface energy on the created/healed new *surfaces* in the elastomer. By construction, the proposed theory can be thought of as a natural generalization of the phase-field approximation (Bourdin et al., 2000; 2008) of the variational theory of brittle fracture introduced in Francfort and Marigo (1998) that accounts for the additional three general physical attributes specific to elastomers:

i. The nucleation of fracture does not necessarily occur in regions where the strain energy concentrates. Instead, because of the typical near incompressibility of elastomers, fracture may nucleate in regions where the hydrostatic stress concentrates;

ii. Fracture is not necessarily a purely dissipative and irreversible process. Instead, fractured surfaces may store energy and healing (partial or complete) is allowed; and

iii. The resistance of elastomers to fracture and to healing is not characterized by a material constant. Instead, it is characterized by a material function that depends on the cumulative history of fracture and healing.

The organization of the paper is as follows. In Sections 2 and 3, we construct the theory of fracture and healing of elastomers in N space dimensions. We do so by identifying elastic deformations[3] of the bulk and surface energy storage on the internal cracks created through the forward phase transition (i.e., fracture) as the mechanisms by which elastomers can store energy. We consider further that both the forward and the reverse (i.e., healing) phase transition may incur energy dissipation. These ideas are first cast in Section 2 within the variational setting introduced in Francfort and Marigo (1998). The Euler-Lagrange equations that stem from a time discretization of this variational theory are then generalized and rendered continuous in time in Section 3, so as to account for all three physical attributes i, ii, iii identified above. This generalization constitutes the complete form of the theory.[4]

From an applications point of view, the theory amounts to solving a system of two coupled and nonlinear partial differential equations (PDEs) — given by Eqs. (20) and (21) — with unknowns the deformation field $\mathbf{y}$ and an order parameter, or phase-field variable, z. Section 4 introduces a finite-element scheme aimed at producing numerical solutions for these equations in the physically relevant contexts of $N = 2$ and 3 space dimensions. Specifically, the equations are recast in weak form in Subsection 4.1, then discretized in time and space in Subsections 4.2 and 4.3. Finally, the solver utilized to generate numerical solutions for the set of nonlinear algebraic equations resulting from the discretizations is discussed in Subsection 4.4. The proposed numerical scheme employs a non-conforming low-order finite-element discretization together with an implicit gradient flow solver that efficiently resolve the challenges of dealing with large deformations, the near incompressibility typical of elastomers, and the large changes in the deformation field that can ensue locally in space and time from the nucleation of fracture. The performance of the scheme in terms of accuracy and stability is illustrated by comparison to two benchmark problems in Section 5.

In Section 6, we explore the descriptive capabilities of the theory by carrying out simulations of the so-called Gent-Park experiment for silicone elastomers with various fracture and healing properties. The main

---

[3]In addition to elastic deformations, viscous deformations are likely to play a role in the nucleation of cavities/cracks in elastomers (Kumar et al., 2017), as well as in their ensuing growth and interactions (see, e.g., Mullins, 1959; Andrews, 1963). In this work we shall restrict attention to the basic case of elastic deformations.

[4]Here, it is fitting to mention that the idea of viewing fracture as a phase transition seems to date back to the 1970s, when, as further elaborated in Truskinovsky (1996), it naturally emerged in the work of Ericksen (1975). That line of thought continued, but mostly in the atomistic study of fracture in crystalline solids (see, e.g., Gao and Klein, 1998; Braides et al., 1999).

Let us also mention that an increasing number of authors have proposed numerical implementations of the related regularized theory of fracture of Bourdin et al. (2000) in the setting of finite deformations (see, e.g., Del Piero et al., 2007; Miehe and Schänzel, 2014; Hesch and Weinberg, 2014; Henao et al., 2016). However, those were, consciously or not, only concerned with highly compressible solids, which avoids numerical intricacies such as volumetric locking.

objectives of these simulations are to gain quantitative insight into the geometric and constitutive inputs that dominate the nucleation and the propagation of fracture and healing, and to confront this insight with the recent experiments at high spatio-temporal resolution of Poulain et al. (2017). This is done in Section 7, where we also record a few final comments.

2. Fracture and healing of elastomers as a solid-to-solid phase transition: a first variational phase-field theory

In Subsections 2.1 through 2.3, we begin by presenting the relevant kinematics of the problem, the mechanisms by which elastomers can store and dissipate energy through deformation, fracture, and healing, as well as the relevant boundary conditions and source terms. In Subsection 2.4, we then present a first pass at the proposed theory. The focus there is on accounting for the physical attribute *ii* identified in the Introduction, namely, that fracture in elastomers is not necessarily a purely dissipative and irreversible process, but that, instead, fractured surfaces may store energy and healing is allowed. We accomplish this through a generalization of the phase-field approximation (Bourdin et al., 2000; 2008) of the variational theory of brittle fracture introduced in Francfort and Marigo (1998) that allows for healing. The incorporation of the additional physical attributes *i* and *iii* is addressed in Section 3.

2.1. Kinematics

Consider an elastomer that occupies in its initial configuration (at time $t = 0$) a bounded domain $\Omega_0 \subset \mathbb{R}^N$, with boundary $\partial \Omega_0$ and unit outward normal $\mathbf{N}$. We identify material points by their initial position vector $\mathbf{X} \in \Omega_0$. At a later time $t \in (0, T]$, due to externally applied "loads" described below, the position vector $\mathbf{X}$ of a material point moves to a new position specified by $\mathbf{x} = \mathbf{y}(\mathbf{X}, t)$, where $\mathbf{y}$ is a mapping from Ω_0 to the current configuration $\Omega(t)$, also contained in $\mathbb{R}^N$. We consider only invertible deformations, and write the deformation gradient field at $\mathbf{X}$ and t as

$$\mathbf{F}(\mathbf{X}, t) = \nabla \mathbf{y}(\mathbf{X}, t).$$

To this, we adjoin an order parameter, or phase-field variable,

$$z(\mathbf{X}, t),$$

which serves as a marker for the two phases in the elastomer. Specifically, we identify the regions that are occupied by the original elastomer with the value of $z = 1$ and the regions occupied by the fractured elastomer featuring vanishingly small stiffness with $z = 0$. In a sharp interface formulation, the field z would only take the value of 1 or 0 at any given material point and hence would be discontinuous at interfaces separating the regions occupied by the two different phases. In this work, we adopt a regularized
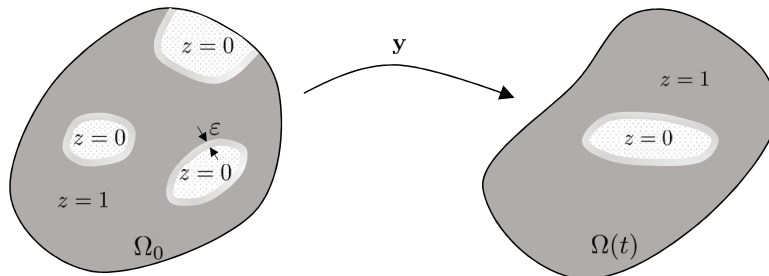

Figure 1: Schematics of an elastomer in its initial configuration at time $t = 0$ and in a deformed configuration, described by the mapping $\mathbf{y}(\mathbf{X}, t)$, at a later time $t > 0$. The schematics also show the coexistence and evolution of the two phases, namely, the original elastomer wherein $z(\mathbf{X}, t) = 1$ and the fractured elastomer featuring vanishingly small stiffness wherein $z(\mathbf{X}, t) = 0$, as well as the thin inter-phase regions of length scale ε separating them, wherein $0 < z(\mathbf{X}, t) < 1$.

4

formulation featuring diffuse interfaces in which the phase-field variable z is allowed to vary smoothly from 1 to 0 over thin inter-phase regions of length scale ε. Figure 1 shows schematics of an elastomer in its initial configuration and at a later time, illustrating the coexistence and evolution of the two solid phases — the original elastomer and the fractured elastomer — and the thin inter-phase regions separating them.

2.2. The mechanisms of energy storage and energy dissipation

The stored elastic energy of the original elastomer. We wish to deal with compressible as well as with nearly incompressible elastomers. To that effect, we assume that the elastic response of the original elastomer can be characterized by a free-energy density of the form

$$W(\mathbf{F}) + \kappa\, g(\mathbf{F}). \tag{1}$$

Material frame indifference requires that

$$W(\mathbf{Q}\mathbf{F}) = W(\mathbf{F}), \; g(\mathbf{Q}\mathbf{F}) = g(\mathbf{F})$$

for all $\mathbf{Q} \in Orth^+$ and arbitrary $\mathbf{F}$. A strong ellipticity condition is also imposed, namely,

$$\frac{\partial^2 W}{\partial F_{ij}\partial F_{kl}}(\mathbf{F})\, A_i A_k b_j b_l + \kappa\, \frac{\partial^2 g}{\partial F_{ij}\partial F_{kl}}(\mathbf{F})\, A_i A_k b_j b_l > 0$$

for all unit vectors $\mathbf{A}$ and $\mathbf{b}$ and arbitrary $\mathbf{F}$. For mathematical well-posedness, we additionally assume that the function W satisfies the growth condition

$$W(\mathbf{F}) \to C|\mathbf{F}|^p \quad \text{as} \quad |\mathbf{F}| \to \infty \tag{2}$$

for some real exponent $p > 1$ and positive constant C (with unit *force/length^{N-1}*), where $|\mathbf{F}|$ is the Frobenius norm $\sqrt{\mathbf{F} \cdot \mathbf{F}} = \sqrt{F_{ij}F_{ij}}$. Further, κ in (1) is a non-negative material parameter (with unit *force/length^{N-1}*) that measures the compressibility of the elastomer: it is defined so that, as $\kappa \to +\infty$, the elastomer becomes incompressible and its free-energy density (1) reduces to

$$\begin{cases} W(\mathbf{F}) & \text{if } \det \mathbf{F} = 1 \\ +\infty & \text{else} \end{cases}.$$

The following isotropic free-energy density (Lopez-Pamies, 2010) is a particular template that will be relied upon in comparisons with experiments further below:

$$\begin{cases} W(\mathbf{F}) = \sum_{r=1}^2 \dfrac{N^{1-\beta_r}}{2\beta_r}\mu_r \left[(\mathbf{F} \cdot \mathbf{F})^{\beta_r} - N^{\beta_r} \right] - \sum_{r=1}^2 \mu_r \ln(\det \mathbf{F}) \\ g(\mathbf{F}) = \dfrac{1}{2}\left(\det \mathbf{F} - 1\right)^2 \end{cases}, \tag{3}$$

where, again, N stands for the space dimension, and where β_r, μ_r $(r = 1, 2)$ are real-valued material parameters (unitless and with unit *force/length^{N-1}*, respectively).

The stored elastic energy of the fractured elastomer and the inter-phase regions. For definiteness, we take the elastic response of the fractured elastomer featuring vanishingly small stiffness, for which the phase-field variable $z = 0$, and of the thin inter-phase regions, for which the phase-field variable $z \in (0,1)$, to be characterized by the free-energy density

$$W_{\mathcal{F}}(\mathbf{F}, z) = (z^2 + \eta_W)W(\mathbf{F}) + (z^2 + \eta_\kappa)\kappa\, g(\mathbf{F}) \tag{4}$$

with positive real numbers $\eta_\kappa \leq \eta_W \ll 1$.

5

The stored surface energy of the inter-phase regions. Besides storing energy through their elastic deformation, the thin inter-phase regions may also store "surface" energy. We associate to such an additional storage mechanism the free-energy density

$$W_{\mathcal{S}}(z) = k_{\mathcal{S}}\mathcal{S}_{\varepsilon}(z) \quad \text{with} \quad \mathcal{S}_{\varepsilon}(z) = \frac{3}{8}\left(\frac{1-z}{\varepsilon} + \varepsilon\, \nabla z \cdot \nabla z\right), \tag{5}$$

where, for now, $k_{\mathcal{S}}$ is taken to be a material constant (with unit $force/length^{N-2}$).

The dissipated energy by the forward and reverse phase transitions. Moreover, both the forward and the reverse phase transitions — that is, again, the fracturing and the healing — may incur dissipation of energy. We associate to this process the dissipation density function $\mathcal{D}(z - z(t); z)$, where

$$\mathcal{D}(Z; z) := \left(k_{\mathcal{F}}1_{\{Z>0\}} - k_{\mathcal{H}}1_{\{Z<0\}}\right)\mathcal{S}_{\varepsilon}(z), \tag{6}$$

$k_{\mathcal{F}}, k_{\mathcal{H}}$ are, for now, also material constants (with unit $force/length^{N-2}$), and 1_A denotes the characteristic function of the set A. For later use we define

$$k_{\mathcal{D}}(Z) := k_{\mathcal{F}}1_{\{Z>0\}} - k_{\mathcal{H}}1_{\{Z<0\}}. \tag{7}$$

Remark 1. The expression (5) is consistent with Griffith's approach to fracture (Griffith, 1921), in that it states that the surface energy stored in the solid is proportional to the surface area that the thin inter-phase regions would occupy in the limit as $\varepsilon \to 0$. Indeed, the expression for $\mathcal{S}_{\varepsilon}$ in (5) is one of a plethora of possible N-dimensional volume density functions that can be used to approximate the area of $(N-1)$–dimensional surfaces contained in N-dimensional domains; see, e.g., Chapter 4 in Braides (1998). The specific form (5) has the merit that it is mathematically simple, it leads to sharp transitions of the phase-field variable from $z = 1$ to $z = 0$, and possesses a number of other theoretical advantages over more conventional forms such as, for instance,

$$\mathcal{S}_{\varepsilon}(z) = \frac{1}{2}\left(\frac{(1-z)^2}{\varepsilon} + \varepsilon\, \nabla z \cdot \nabla z\right).$$

For a discussion of these, we refer the reader to Pham et al. (2011) and Sicsic and Marigo (2013); see also Maurini et al. (2013) and Mesgarnejad et al. (2015).

The choice of dissipation density function (6) is also consistent with Griffith's approach to fracture, as both terms in (6) state in essence that the energy dissipated in fracturing or in healing is proportional to the created or healed surface area, that is that which the region $z < 1$ would reduce to in the limit as $\varepsilon \to 0$.

2.3. Boundary conditions and source terms

We now specify the externally applied "loads". They comprise both boundary data and source terms in the bulk.

Thus, we take that complementary portions $\partial\Omega_0^{\mathbf{y}}$ and $\partial\Omega_0^{\mathbf{S}} = \partial\Omega_0 \backslash \partial\Omega_0^{\mathbf{y}}$ of the boundary $\partial\Omega_0$ are subjected, respectively, to a prescribed deformation and a prescribed nominal traction

$$\boldsymbol{\xi}(\mathbf{X}, t), \quad (\mathbf{X}, t) \in \partial\Omega_0^{\mathbf{y}} \times [0, T] \qquad \text{and} \qquad \boldsymbol{\sigma}(\mathbf{X}, t), \quad (\mathbf{X}, t) \in \partial\Omega_0^{\mathbf{S}} \times [0, T].$$

Moreover, the boundary condition on the phase-field variable is prescribed to be given by the Neumann boundary condition

$$\nabla z(\mathbf{X}, t) \cdot \mathbf{N} = 0, \quad (\mathbf{X}, t) \in \partial\Omega_0 \times [0, T].$$

This implies, as one might expect on physical grounds, that the fracturing and the healing of the elastomer is solely driven by the mechanical loads applied to it, and not by the direct imposition of a phase transition stimulus on its boundary.

Throughout Ω_0, the solid is also subjected to a body force

$$\mathbf{b}(\mathbf{X}, t), \qquad (\mathbf{X}, t) \in \Omega_0 \times [0, T].$$

2.4. A first variational phase-field theory

At this stage, we are in a position to formulate the first pass at the theory. For this, take the Griffith viewpoint that the forward and reverse phase transitions are driven by the competition between strain energy in the bulk and surface energy on the created/healed new surfaces in the elastomer. Then, by extending the variational approach of brittle fracture (see, in particular, Francfort and Marigo, 1998; Giacomini, 2005; Bourdin et al., 2008) to allow for healing, the deformation field $\mathbf{y}(\mathbf{X}, t)$ and the phase field $z(\mathbf{X}, t)$ should satisfy the following two-pronged criterion:

Global Stability. At each time $t \in [0, T]$, the pair $\mathbf{y}(\mathbf{X}, t), z(\mathbf{X}, t)$ is a minimizer of

$$\int_{\Omega_0} \{W_{\mathcal{F}}(\nabla\boldsymbol{\psi}, \omega) + W_{\mathcal{S}}(\omega)\}(\mathbf{X})\, \mathrm{d}\mathbf{X} + \int_{\Omega_0} \mathcal{D}(\omega - z(t); \omega)(\mathbf{X})\, \mathrm{d}\mathbf{X} - \int_{\Omega_0} \mathbf{b}(\mathbf{X}, t) \cdot \boldsymbol{\psi}(\mathbf{X})\, \mathrm{d}\mathbf{X} - \int_{\partial\Omega_0^{\mathbf{s}}} \boldsymbol{\sigma}(\mathbf{X}, t) \cdot \boldsymbol{\psi}(\mathbf{X})\, \mathrm{d}\mathbf{X}$$

among all pairs $(\boldsymbol{\psi}, \omega)$ with $\det \nabla\boldsymbol{\psi}(\mathbf{X}) > 0$, $\boldsymbol{\psi}(\mathbf{X}) = \boldsymbol{\xi}(\mathbf{X}, t)$ on $\partial\Omega_0^{\mathbf{y}}$, and $0 \le \omega(\mathbf{X}) \le 1$;

Energy balance. Setting

$$E(t) := \int_{\Omega_0} \{W_{\mathcal{F}}(\nabla\mathbf{y}, z) + W_{\mathcal{S}}(z)\}(\mathbf{X}, t)\, \mathrm{d}\mathbf{X} + \int_0^t \int_{\Omega_0} \mathcal{D}(\dot{z}(\mathbf{X}, s); z(\mathbf{X}, s))\, \mathrm{d}\mathbf{X}\, \mathrm{d}s -$$
$$\int_{\Omega_0} \mathbf{b}(\mathbf{X}, t) \cdot \mathbf{y}(\mathbf{X}, t)\, \mathrm{d}\mathbf{X} - \int_{\partial\Omega_0^{\mathbf{s}}} \boldsymbol{\sigma}(\mathbf{X}, t) \cdot \mathbf{y}(\mathbf{X}, t)\, \mathrm{d}\mathbf{X},$$

we also have

$$\frac{\mathrm{d}E}{\mathrm{d}t}(t) = \int_{\partial\Omega_0^{\mathbf{y}}} \frac{\partial W_{\mathcal{F}}}{\partial \mathbf{F}}(\nabla\mathbf{y}, z)\mathbf{N} \cdot \frac{\mathrm{d}\boldsymbol{\xi}}{\mathrm{d}t}(\mathbf{X}, t)\, \mathrm{d}\mathbf{X} - \int_{\Omega_0} \frac{\mathrm{d}\mathbf{b}}{\mathrm{d}t}(\mathbf{X}, t) \cdot \mathbf{y}(\mathbf{X}, t)\, \mathrm{d}\mathbf{X}.$$

For a detailed discussion of the applicability of this kind of variational evolution to a large class of dissipative phenomena that go beyond brittle fracture, the reader is referred to e.g. Mielke (2003), Mielke and Theil (2004), Hackl and Fischer (2008), or Hackl et al. (2011).

Discussion around the existence of a minimizing pair $\mathbf{y}(\mathbf{X}, t), z(\mathbf{X}, t)$ for the previous formulation should then be the next step which would take us beyond the scope of the present contribution. Instead, we will merely assume that existence has been established through an implicit Euler scheme. In other words, having partitioned the time interval of interest $[0, T]$ into the discrete times $0 = t^0, t^1, ..., t^m, t^{m+1}, ..., t^M = T$, we propose to solve, for any $m \in \{0, ..., M\}$, the following minimization problem:

Discrete Global Stability. Assuming z^{m-1} is known, find $\mathbf{y}^m(\mathbf{X}), z^m(\mathbf{X})$ a minimizer of

$$\int_{\Omega_0} \{W_{\mathcal{F}}(\nabla\boldsymbol{\psi}, \omega) + W_{\mathcal{S}}(\omega)\}(\mathbf{X})\, \mathrm{d}\mathbf{X} + \int_{\Omega_0} k_{\mathcal{D}}(\omega - z^{m-1})\mathcal{S}_\varepsilon(\omega)(\mathbf{X})\, \mathrm{d}\mathbf{X}$$
$$- \int_{\Omega_0} \mathbf{b}(\mathbf{X}, t^m) \cdot \boldsymbol{\psi}(\mathbf{X})\, \mathrm{d}\mathbf{X} - \int_{\partial\Omega_0^{\mathbf{s}}} \boldsymbol{\sigma}(\mathbf{X}, t^m) \cdot \boldsymbol{\psi}(\mathbf{X})\, \mathrm{d}\mathbf{X} \quad (8)$$

among all pairs $(\boldsymbol{\psi}, \omega)$ with $\det \nabla\boldsymbol{\psi}(\mathbf{X}) > 0$, $\boldsymbol{\psi}(\mathbf{X}) = \boldsymbol{\xi}(\mathbf{X}, t^m)$ on $\partial\Omega_0^{\mathbf{y}}$, and $0 \le \omega(\mathbf{X}) \le 1$. Note that, for the first time, we have to introduce an artificial discrete negative time t^{-1} at which time

$$z^{-1}(\mathbf{X}) \equiv 1 \text{ on } \Omega_0. \quad (9)$$

Staggered algorithm as a proxy for the minimization of (8). The minimization process in (8) is non trivial because, although the functional is convex in $\nabla\omega$ at fixed $\boldsymbol{\psi}$ and ω, it is not convex in the pair $\boldsymbol{\psi}, \omega$, nor even in ω at fixed $\boldsymbol{\psi}$. There is no fool-proof strategy for a successful implementation of the search for a global minimizer to (8), even though we do know, through a judicious application of the direct method of

the Calculus of Variations,[5] that such a minimizer exists. Rather numerical *savoir faire* seems to privilege alternate minimization because it takes advantage of the partial convexity properties of the functional. We thus propose the following alternate minimization algorithm at time t^m: Find, for $r = 1, ..., \mathtt{I}_m$ ($\mathtt{I}_m$ being the number of iterations at time t^m), $\mathbf{y}^{m,r}(\mathbf{X}), z^{m,r}(\mathbf{X})$ such that

- For the initial increment

$$\mathbf{y}^{m,0}(\mathbf{X}) = \mathbf{y}^{m-1}(\mathbf{X}) \text{ and } z^{m,0}(\mathbf{X}) = z^{m-1}(\mathbf{X}); \tag{10}$$

- $\mathbf{y}^{m,r}(\mathbf{X})$ minimizes

$$\int_{\Omega_0} W_{\mathcal{F}}(\nabla\boldsymbol{\psi}, z^{m,r-1})(\mathbf{X}) \, \mathrm{d}\mathbf{X} - \int_{\Omega_0} \mathbf{b}(\mathbf{X}, t^m) \cdot \boldsymbol{\psi}(\mathbf{X}) \, \mathrm{d}\mathbf{X} - \int_{\partial\Omega_0^{\mathbf{S}}} \boldsymbol{\sigma}(\mathbf{X}, t^m) \cdot \boldsymbol{\psi}(\mathbf{X}) \, \mathrm{d}\mathbf{X} \tag{11}$$

  among all $\boldsymbol{\psi}$'s with $\det \nabla\boldsymbol{\psi}(\mathbf{X}) > 0$, $\boldsymbol{\psi}(\mathbf{X}) = \boldsymbol{\xi}(\mathbf{X}, t^m)$ on $\partial\Omega_0^{\mathbf{y}}$;

- $z^{m,r}(\mathbf{X})$ minimizes

$$\int_{\Omega_0} \{W_{\mathcal{F}}(\nabla\mathbf{y}^{m,r}, \omega) + W_{\mathcal{S}}(\omega)\}(\mathbf{X}) \, \mathrm{d}\mathbf{X} + \int_{\Omega_0} k_{\mathcal{D}}(z^{m,r-1} - z^{m-1})\mathcal{S}_{\varepsilon}(\omega)(\mathbf{X}) \, \mathrm{d}\mathbf{X} \tag{12}$$

  among all ω's with $0 \leq \omega(\mathbf{X}) \leq 1$; and

- Set $\mathbf{y}^m := \mathbf{y}^{m,\mathtt{I}_m}$ and $z^m := z^{m,\mathtt{I}_m}$.

Note that the proposed alternate minimization algorithm renders the dependence of $k_{\mathcal{D}}$ on z explicit, precisely because it replaces $k_{\mathcal{D}}(\omega - z^{m-1})$ by $k_{\mathcal{D}}(z^{m,r-1} - z^{m-1})$. This is essential to assert convexity of the functional involved in (12) and to allow for the derivation of the associated Euler-Lagrange equations below.

Remark 2. Keeping an implicit formulation for the discretized $k_{\mathcal{D}}(\omega - z(t))$ in the form $k_{\mathcal{D}}(\omega - z^{m-1})$ would be possible at the level of the variational formulation (12) but it would modify the associated Euler-Lagrange equations (13)–(14) below.

With this alternate minimization at hand, we are then at liberty to write the resulting Euler-Lagrange equations that such alternate minimizers should satisfy. These are

$$\begin{cases} \operatorname{Div}\left[((z^{m,r-1})^2 + \eta_W)\dfrac{\partial W}{\partial \mathbf{F}}(\nabla\mathbf{y}^{m,r}) + ((z^{m,r-1})^2 + \eta_\kappa)\kappa\dfrac{\partial g}{\partial \mathbf{F}}(\nabla\mathbf{y}^{m,r})\right] + \mathbf{b}(\mathbf{X}, t^m) = \mathbf{0}, \quad \mathbf{X} \in \Omega_0 \\[2mm] \qquad\qquad \det \nabla\mathbf{y}^{m,r}(\mathbf{X}) > 0, \quad \mathbf{X} \in \Omega_0, \quad \mathbf{y}^{m,r}(\mathbf{X}) = \boldsymbol{\xi}(\mathbf{X}, t^m), \quad \mathbf{X} \in \partial\Omega_0^{\mathbf{y}} \\[2mm] \left[((z^{m,r-1})^2 + \eta_W)\dfrac{\partial W}{\partial \mathbf{F}}(\nabla\mathbf{y}^{m,r}) + ((z^{m,r-1})^2 + \eta_\kappa)\kappa\dfrac{\partial g}{\partial \mathbf{F}}(\nabla\mathbf{y}^{m,r})\right]\mathbf{N} = \boldsymbol{\sigma}(\mathbf{X}, t^m), \quad \mathbf{X} \in \partial\Omega_0^{\mathbf{S}} \end{cases} \tag{13}$$

---

[5]We will refrain from mathematical digressions in this paper and trust that the concerned reader will readily acquiesce in our assertion.

and

$$
\begin{cases}
\dfrac{3}{4}\mathrm{Div}\left[\varepsilon(k_{\mathcal{S}} + k_{\mathcal{D}}(z^{m,r-1} - z^{m-1}))\nabla z^{m,r}\right] = \\[2ex]
\quad 2z^{m,r}\left(W(\nabla\mathbf{y}^{m,r}) + \kappa g(\nabla\mathbf{y}^{m,r})\right) - \dfrac{3\left(k_{\mathcal{S}} + k_{\mathcal{D}}(z^{m,r-1} - z^{m-1})\right)}{8\varepsilon}, \\[2ex]
\qquad\qquad \text{if } 0 < z^{m,r}(\mathbf{X}) < 1, \quad \mathbf{X} \in \Omega_0 \\[3ex]
\dfrac{3}{4}\mathrm{Div}\left[\varepsilon(k_{\mathcal{S}} + k_{\mathcal{D}}(z^{m,r-1} - z^{m-1}))\nabla z^{m,r}\right] \geq (\text{ resp. } \leq) \\[2ex]
\quad 2z^{m,r}\left(W(\nabla\mathbf{y}^{m,r}) + \kappa g(\nabla\mathbf{y}^{m,r})\right) - \dfrac{3\left(k_{\mathcal{S}} + k_{\mathcal{D}}(z^{m,r-1} - z^{m-1})\right)}{8\varepsilon}, \\[2ex]
\qquad\qquad \text{if } z^{m,r}(\mathbf{X}) = 1(\text{ resp. } = 0), \quad \mathbf{X} \in \Omega_0 \\[3ex]
\qquad\qquad \nabla z^{m,r} \cdot \mathbf{N} = 0, \quad \mathbf{X} \in \partial\Omega_0.
\end{cases}
\tag{14}
$$

Note that the Euler-Lagrange equation (13) is nothing more than the balance of linear momentum for the elastomer, while the coupled Euler-Lagrange equation (14) is the equation that governs the evolution of the phase-field variable.

Time-continuous version of the Euler-Lagrange equations (13)–(14). If we were only concerned with accounting for the possibility of healing, then the next step would consist in working out the details of the numerical implementation of (13)–(14). As made clear from the outset, however, the situation is not so simple because we are yet to address the nucleation of fracture in regions of the elastomer where the hydrostatic stress concentrates and the evolution of the fracture and healing properties in regions of the elastomer that experience healing. At this point, it is not clear whether it is possible to account for these additional physical attributes within the confines of a variational setting. Nonetheless, such attributes can be incorporated at the level of the Euler-Lagrange equations (13)–(14).

For clarity of exposition, we will not implement the generalizations on (13)–(14), but rather on the following time-continuous version

$$
\begin{cases}
\mathrm{Div}\left[(z^2 + \eta_W)\dfrac{\partial W}{\partial\mathbf{F}}(\nabla\mathbf{y}) + (z^2 + \eta_\kappa)\kappa\dfrac{\partial g}{\partial\mathbf{F}}(\nabla\mathbf{y})\right] + \mathbf{b}(\mathbf{X},t) = \mathbf{0}, \quad (\mathbf{X},t) \in \Omega_0 \times [0,T] \\[2ex]
\det\nabla\mathbf{y}(\mathbf{X},t) > 0, \quad (\mathbf{X},t) \in \Omega_0 \times [0,T], \quad \mathbf{y}(\mathbf{X},t) = \boldsymbol{\xi}(\mathbf{X},t), \quad (\mathbf{X},t) \in \partial\Omega_0^{\mathbf{y}} \times [0,T] \\[2ex]
\left[(z^2 + \eta_W)\dfrac{\partial W}{\partial\mathbf{F}}(\nabla\mathbf{y}) + (z^2 + \eta_\kappa)\kappa\dfrac{\partial g}{\partial\mathbf{F}}(\nabla\mathbf{y})\right]\mathbf{N} = \boldsymbol{\sigma}(\mathbf{X},t), \quad (\mathbf{X},t) \in \partial\Omega_0^{\mathbf{S}} \times [0,T]
\end{cases}
\tag{15}
$$

and

$$
\begin{cases}
\dfrac{3}{4}\mathrm{Div}\left[\varepsilon k(\dot{z})\nabla z\right] = 2z\left(W(\nabla\mathbf{y}) + \kappa g(\nabla\mathbf{y})\right) - \dfrac{3k(\dot{z})}{8\varepsilon}, \\[2ex]
\qquad \text{if } 0 < z(\mathbf{X},t) < 1, \quad (\mathbf{X},t) \in \Omega_0 \times [0,T] \\[3ex]
\dfrac{3}{4}\mathrm{Div}\left[\varepsilon k(\dot{z})\nabla z\right] \geq (\text{ resp. } \leq)2z\left(W(\nabla\mathbf{y}) + \kappa g(\nabla\mathbf{y})\right) - \dfrac{3k(\dot{z})}{8\varepsilon}, \\[2ex]
\qquad \text{if } z(\mathbf{X},t) = 1(\text{ resp. } = 0), \quad (\mathbf{X},t) \in \Omega_0 \times [0,T] \\[3ex]
\qquad \nabla z \cdot \mathbf{N} = 0, \quad (\mathbf{X},t) \in \partial\Omega_0 \times [0,T].
\end{cases}
\tag{16}
$$

9

where we have introduced the notation

$$k(\dot{z}) = \begin{cases} k_{\mathcal{S}} + k_{\mathcal{F}} & \text{if} \quad \dot{z} \leq 0 \\ \\ k_{\mathcal{S}} - k_{\mathcal{H}} & \text{if} \quad \dot{z} > 0 \end{cases} . \tag{17}$$

Remark 3. The above time-continuous equations have reintroduced an implicit dependence of k upon the phase-field variable z and thereby taken us away from the variational viewpoint to the extent that the new system (15)–(16) is not the Euler-Lagrange equation associated with the global stability principle in the time continuous evolution. Nor is its time discretization proposed in Subsection 4.2 below the Euler-Lagrange system associated with the time discretization (8) of that principle.

3. Fracture and healing of elastomers as a solid-to-solid phase transition: the complete proposed theory

In this section, as the final step in the construction of the theory, we generalize equations (16)–(17) to account for the additional physical attributes *i* and *iii* identified in the Introduction, namely, that fracture in elastomers typically nucleates in regions where the hydrostatic stress concentrates (see Subsection 3.1) and that the resistance of elastomers to fracture and to healing evolves in regions that experience healing (see Subsection 3.2). The resulting complete theory is presented in Subsection 3.3.

3.1. Nucleation of fracture

When deformed, because of their typical near incompressibility, elastomers are prone to feature regions where the hydrostatic part of the stress is very large while, at the same time, the strain energy is comparatively small (because the strain is small). This has been long known to be the case, for instance, near reinforcing fillers in filled elastomers; see, e.g., the analysis in Lefèvre et al. (2015). As outlined in the Introduction, it is precisely in those regions that the nucleation of internal fracture often occurs first. Physically, this can be understood at once from the recognition that the concentration of large hydrostatic stresses — in spite of the absence of strain — triggers the growth of the underlying microscopic defects, and thus, the nucleation of fracture at macroscopic length scales.

The above realization indicates that nucleation cannot be captured through a balance *à la* Griffith between strain energy in the bulk and surface energy on the created/healed new surfaces in the elastomer; indeed, such a balance would fail to identify areas of large hydrostatic stresses but small strain because their contribution to the strain energy is minute. Instead, it suggests the addition of an external driving force[6], say $-c_{\mathsf{e}}$, in the right hand-side of (16) that should be proportional to the hydrostatic part of the stress. At the same time, it should also be negligible when the elastomer is highly compressible and/or highly stretched, for then the strain energy is no longer comparatively small. Accordingly, in this work we shall take that force to be given by

$$c_{\mathsf{e}}(\mathbf{X}, t) = -\gamma \, z \, \frac{3^{\frac{p}{2}}}{|\mathbf{F}|^p} \left(\frac{\kappa}{3 \det \mathbf{F}} \mathbf{F} \cdot \frac{\partial g}{\partial \mathbf{F}}(\mathbf{F}) \right). \tag{18}$$

Notice that the term inside the parenthesis in (18) is nothing more than the hydrostatic part of the Cauchy stress $\mathbf{T} = (\det \mathbf{F})^{-1} \mathbf{S} \mathbf{F}^T$ associated with the compressibility parameter κ. The preceding quotient is a normalized measure of stretch. It takes the value of 1 in the absence of stretch, that is when $\mathbf{F} \in Orth^+$. As the stretch increases, the quotient — and hence the force c_{e} — approaches zero with the inverse of the norm $|\mathbf{F}|^p$ that describes the growth (2) of the stored-energy function W at large stretches. Notice as well that the force (18) vanishes within the fractured regions of the elastomer, where $z = 0$, which is consistent with physical expectations. Finally, the coefficient γ in (18) is a non-negative unitless parameter whose selection

---

[6]In the parlance of configurational forces, see Remark 7 below, the macroscopic driving force c_{e} is called a configurational external force.

depends *inter alia* on the compressibility of the elastomer. For nearly incompressible elastomers γ should be selected to be of order 1, while for highly compressible elastomers γ should be selected to be vanishingly small.

At this point, it is important to emphasize that the specific choice (18) for the external force $c_{\mathbf{e}}$ is primarily based on macroscopic experimental observations, and thus, that it is purely phenomenological. In the Appendix, we present some evidence that sheds light on its microscopic origins. This points specifically to the dependence of the parameter γ on the compressibility of the elastomer, as well as on the size of the microscopic defects from which fracture initiates.

3.2. Evolution of the fracture and healing properties

The material coefficients $k_{\mathcal{S}}, k_{\mathcal{F}}, k_{\mathcal{H}}$ have been construed thus far as material constants; this interpretation is certainly appropriate for many polycrystalline and glassy solids for which one would usually set $k_{\mathcal{S}} = 0, k_{\mathcal{F}} = G_c, k_{\mathcal{H}} = 0$, where G_c would be the critical energy release rate of the given solid. However, recent experiments by Ravi-Chandar (2016) on a variety of silicone elastomers seem to point to an evolution of these coefficients in terms of the cumulative history of fracture and healing. In particular, the experiments show that the resistance of an elastomer to fracture and to healing can evolve at a material point $\mathbf{X}$ after every *complete cycle* of fracturing and healing at that point. *Id est*, after every cycle in which the phase-field variable changes from $z(\mathbf{X}, t_1) = 1$ to $z(\mathbf{X}, t_2) = 0$ and back to $z(\mathbf{X}, t_3) = 1$ along a given loading path, at which points the molecular structure of the elastomer may adopt a different geometric arrangement and/or form different chemical bonds.

To describe the above observed behavior, we introduce the memory variables

$$\alpha(\mathbf{X}, t) = \int_0^t |\dot{z}(\mathbf{X}, \tau)| \, \mathrm{d}\tau \qquad \text{and} \qquad t^*(\mathbf{X}, t) = \sup \{\tau : \tau < t \text{ and } z(\mathbf{X}, \tau) = 1\}, \qquad (19)$$

and postulate that

$$k_{\mathcal{S}} := k_{\mathcal{S}}^0 + H_{\mathcal{S}} \left(\alpha(\mathbf{X}, t^*(\mathbf{X}, t))\right),$$
$$k_{\mathcal{F}} := k_{\mathcal{F}}^0 + H_{\mathcal{F}} \left(\alpha(\mathbf{X}, t^*(\mathbf{X}, t))\right),$$
$$k_{\mathcal{H}} := k_{\mathcal{H}}^0 + H_{\mathcal{H}} \left(\alpha(\mathbf{X}, t^*(\mathbf{X}, t))\right),$$

where $k_{\mathcal{S}}^0, k_{\mathcal{F}}^0, k_{\mathcal{H}}^0$ are non-negative material constants (with unit *force/length^{N-2}*) and $H_{\mathcal{S}}, H_{\mathcal{F}}, H_{\mathcal{H}}$ are bounded material functions (obviously, also with unit *force/length^{N-2}*) satisfying the condition $H_{\mathcal{S}}(0) = H_{\mathcal{F}}(0) = H_{\mathcal{H}}(0) = 0$ and the lower bound $H_{\mathcal{S}}(t) \geq -k_{\mathcal{S}}^0$ (*idem* for the other two).

3.3. The proposed theory

We are now in a position to formulate the complete theory of fracture and healing of elastomers. Indeed, making use of the above-introduced external force $c_{\mathbf{e}}$ and evolving coefficients $k_{\mathcal{S}}$, $k_{\mathcal{F}}$, $k_{\mathcal{H}}$ in the Euler-Lagrange equations (15)–(16), the following governing equations are generated for the deformation field $\mathbf{y}(\mathbf{X}, t)$ and the phase field $z(\mathbf{X}, t)$ describing the deformation and the nucleation and propagation of fracture and healing of a given elastomer of interest along any given loading path with prescribed deformation $\boldsymbol{\xi}(\mathbf{X}, t)$ on $\partial\Omega_0^{\mathbf{y}}$, prescribed nominal traction $\boldsymbol{\sigma}(\mathbf{X}, t)$ on $\partial\Omega_0^{\mathbf{S}}$, and prescribed body force $\mathbf{b}(\mathbf{X}, t)$ in Ω_0:

$$\begin{cases} \mathrm{Div} \left[(z^2 + \eta_W)\dfrac{\partial W}{\partial \mathbf{F}}(\nabla \mathbf{y}) + (z^2 + \eta_\kappa)\kappa \dfrac{\partial g}{\partial \mathbf{F}}(\nabla \mathbf{y})\right] + \mathbf{b}(\mathbf{X}, t) = \mathbf{0}, \quad (\mathbf{X}, t) \in \Omega_0 \times [0, T] \\[2mm] \det \nabla \mathbf{y}(\mathbf{X}, t) > 0, \quad (\mathbf{X}, t) \in \Omega_0 \times [0, T], \quad \mathbf{y}(\mathbf{X}, t) = \boldsymbol{\xi}(\mathbf{X}, t), \quad (\mathbf{X}, t) \in \partial\Omega_0^{\mathbf{y}} \times [0, T] \\[2mm] \left[(z^2 + \eta_W)\dfrac{\partial W}{\partial \mathbf{F}}(\nabla \mathbf{y}) + (z^2 + \eta_\kappa)\kappa \dfrac{\partial g}{\partial \mathbf{F}}(\nabla \mathbf{y})\right] \mathbf{N} = \boldsymbol{\sigma}(\mathbf{X}, t), \quad (\mathbf{X}, t) \in \partial\Omega_0^{\mathbf{S}} \times [0, T] \end{cases} \qquad (20)$$

and

$$
\begin{cases}
\mathrm{Div}\left[\varepsilon k(\dot{z},\alpha,t^*)\nabla z\right] = \dfrac{8}{3}z\left(W(\nabla\mathbf{y}) + \kappa g(\nabla\mathbf{y})\right) + 4\gamma\,z\,\dfrac{3^{\frac{p-4}{2}}}{|\nabla\mathbf{y}|^p}\left(\dfrac{\kappa}{\det\nabla\mathbf{y}}\nabla\mathbf{y}\cdot\dfrac{\partial g}{\partial\mathbf{F}}(\nabla\mathbf{y})\right) - \dfrac{k(\dot{z},\alpha,t^*)}{2\varepsilon},\\[2mm]
\qquad\qquad \text{if } 0 < z(\mathbf{X},t) < 1, \quad (\mathbf{X},t)\in\Omega_0\times[0,T]\\[4mm]
\mathrm{Div}\left[\varepsilon k(\dot{z},\alpha,t^*)\nabla z\right] \geq (\text{ resp. } \leq)\dfrac{8}{3}z\left(W(\nabla\mathbf{y}) + \kappa g(\nabla\mathbf{y})\right) + 4\gamma\,z\,\dfrac{3^{\frac{p-4}{2}}}{|\nabla\mathbf{y}|^p}\left(\dfrac{\kappa}{\det\nabla\mathbf{y}}\nabla\mathbf{y}\cdot\dfrac{\partial g}{\partial\mathbf{F}}(\nabla\mathbf{y})\right) - \dfrac{k(\dot{z},\alpha,t^*)}{2\varepsilon},\\[2mm]
\qquad\qquad \text{if } z(\mathbf{X},t) = 1(\text{ resp. } = 0), \quad (\mathbf{X},t)\in\Omega_0\times[0,T]\\[4mm]
\qquad\qquad\qquad \nabla z\cdot\mathbf{N} = 0, \quad (\mathbf{X},t)\in\partial\Omega_0\times[0,T]
\end{cases}
\tag{21}
$$

with

$$
k(\dot{z},\alpha,t^*) = \begin{cases}
k_{\mathcal{S}} + k_{\mathcal{F}} = k_{\mathcal{S}}^0 + k_{\mathcal{F}}^0 + H_{\mathcal{S}}\left(\alpha(\mathbf{X},t^*(\mathbf{X},t))\right) + H_{\mathcal{F}}\left(\alpha(\mathbf{X},t^*(\mathbf{X},t))\right) & \text{if } \dot{z}\leq 0\\[2mm]
k_{\mathcal{S}} - k_{\mathcal{H}} = k_{\mathcal{S}}^0 - k_{\mathcal{H}}^0 + H_{\mathcal{S}}\left(\alpha(\mathbf{X},t^*(\mathbf{X},t))\right) - H_{\mathcal{H}}\left(\alpha(\mathbf{X},t^*(\mathbf{X},t))\right) & \text{if } \dot{z}> 0
\end{cases}
\tag{22}
$$

where we recall that $\alpha(\mathbf{X},t)$ and $t^*(\mathbf{X},t)$ stand for the memory variables (19). The following remarks are in order.

Remark 4. *The toughness function $k(\dot{z},\alpha,t^*)$.* The function (22) is the constitutive quantity that describes the resistance, or "toughness", of the elastomer to fracture and to healing. As it will become more apparent below, it can be thought of as a generalization of the usual critical energy release rate G_c when accounting for different constitutive behaviors in fracture ($\dot{z} < 0$) and healing ($\dot{z} > 0$), as well as for the evolution of these constitutive behaviors due to the breaking and possible re-forming of different types of molecular arrangements and/or chemical bonds along a given loading path. We shall refer to $k(\dot{z},\alpha,t^*)$ as the material *toughness function*.

We remark that both branches of the toughness function (22) are the additive combinations of contributions from surface energy storage, characterized by $k_{\mathcal{S}}$, and surface energy dissipation, characterized by $k_{\mathcal{F}}$ for fracture and by $k_{\mathcal{H}}$ for healing.

The branch of $k(\dot{z},\alpha,t^*)$ corresponding to fracture ($\dot{z} < 0$) has an initial value at time $t = 0$ given by $k_{\mathcal{S}}^0 + k_{\mathcal{F}}^0$. This combination is non-negative and equal to the critical energy release rate G_c of the elastomer under consideration[7]. Along a given loading path, the value of $k(\dot{z},\alpha,t^*)$ for the fracture branch may remain constant at $k_{\mathcal{S}}^0 + k_{\mathcal{F}}^0 = G_c$, or may increase or decrease depending on the cumulative history of fracture characterized by the combination of functions $H_{\mathcal{S}}\left(\alpha(\mathbf{X},t^*(\mathbf{X},t))\right) + H_{\mathcal{F}}\left(\alpha(\mathbf{X},t^*(\mathbf{X},t))\right)$ in terms of the memory variables (19). Recent cyclic-loading experiments on silicone elastomers (Ravi-Chandar, 2016) suggest that $H_{\mathcal{S}}\left(\alpha(\mathbf{X},t^*(\mathbf{X},t))\right) + H_{\mathcal{F}}\left(\alpha(\mathbf{X},t^*(\mathbf{X},t))\right) \geq 0$. We will explore this behavior via sample results below.

On the other hand, the branch of $k(\dot{z},\alpha,t^*)$ corresponding to healing ($\dot{z} > 0$) has an initial value given by $k_{\mathcal{S}}^0 - k_{\mathcal{H}}^0$, which is *not* necessarily non-negative. Notice in particular that $k_{\mathcal{S}}^0 - k_{\mathcal{H}}^0 \leq G_c$ with equality holding only when $k_{\mathcal{F}}^0 = k_{\mathcal{H}}^0 = 0$. That is, the initial fracture toughness is equal to the initial healing toughness only when the processes of fracture and healing do not incur energy dissipation. Along a given loading path, the value of $k(\dot{z},\alpha,t^*)$ for the healing branch may remain constant at $k_{\mathcal{S}}^0 - k_{\mathcal{H}}^0$, or may increase or decrease depending on the cumulative history of healing characterized by combination of functions $H_{\mathcal{S}}\left(\alpha(\mathbf{X},t^*(\mathbf{X},t))\right) - H_{\mathcal{H}}\left(\alpha(\mathbf{X},t^*(\mathbf{X},t))\right)$ in terms of the memory variables (19). Much like it is possible for the initial value $k_{\mathcal{S}}^0 - k_{\mathcal{H}}^0$ of $k(\dot{z},\alpha,t^*)$ for the healing branch to be non-positive, the combination

---

[7]Currently, the experimental literature is still divided as to the correct order of magnitude for G_c in standard elastomers. Conventional experiments on macroscopic specimens suggest that $G_c \approx 100$ J/m^2 or even larger (see, e.g., Lake and Thomas, 1967; Gent and Wang, 1991). Experiments on specimens of micron size, on the other hand, suggest that $G_c \approx 0.05$ J/m^2 (see, e.g., Fond et al., 1996).

$H_{\mathcal{S}}\left(\alpha(\mathbf{X}, t^*(\mathbf{X}, t))\right) - H_{\mathcal{H}}\left(\alpha(\mathbf{X}, t^*(\mathbf{X}, t))\right)$ may be non-positive as well. Physically, non-positive values of the toughness function $k(\dot{z}, \alpha, t^*)$ for the healing branch imply that healing is prohibited, or in other words, that fracture is irreversible.

Remark 5. *The competing bulk and surface quantities that drive the phase transition.* The right-hand side of the governing equation (21) makes apparent the precise competition between bulk and surface quantities that drive the nucleation and propagation of fracture and healing in the elastomer. Indeed, we remark that nucleation and propagation of fracture will occur at a material point $\mathbf{X}$ whenever the strain energy, as characterized by $W(\mathbf{F}) + \kappa g(\mathbf{F})$, together with the hydrostatic stress relative to the amount of stretch, as characterized by $\gamma\, 3^{\frac{p-4}{2}}/|\mathbf{F}|^p((\kappa/\det \mathbf{F})\,\mathbf{F} \cdot \partial g(\mathbf{F})/\partial \mathbf{F})$, is sufficiently large relative to the fracture toughness $k(\dot{z}, \alpha, t^*)$ of the elastomer at that material point. By the same token, healing will occur at a material point $\mathbf{X}$ if the same combination of strain energy and stress is sufficiently small relative to the healing toughness at that material point.

In addition to promoting the nucleation of fracture in regions where the hydrostatic stress (relative to the amount of stretch) concentrates, the driving force term $\gamma\, 3^{\frac{p-4}{2}}/|\mathbf{F}|^p((\kappa/\det \mathbf{F})\,\mathbf{F} \cdot \partial g(\mathbf{F})/\partial \mathbf{F})$ in the governing equation (21) also generally prevents (for realistic values of the compressibility parameter κ) the nucleation of fracture in regions featuring compressive states of stress.

Remark 6. *The parameters η_W and η_κ for the case of nearly incompressible elastomers.* The parameters η_W and η_κ introduced in (4) are small positive numbers that serve to quantify the vanishingly small stiffness of the thin regions of the elastomer that have undergone fracture. When dealing with nearly incompressible elastomers, the compressibility parameter κ is typically 10^3 to 10^4 times larger than the smallest component of the initial modulus of elasticity $L_{ijkl} \doteq 1/2(\partial^2 W/\partial F_{ij}\partial F_{kl} + \kappa \partial^2 g/\partial F_{ij}\partial F_{kl})(\mathbf{I})$ of the elastomer under consideration (see, e.g., Bridgman, 1945; Bischoff, 2001). Thus, to ensure that the fractured regions are indeed of vanishingly small stiffness, and, in particular, "empty" of an elastic fluid, the parameter η_κ should be chosen according to the rule

$$\eta_\kappa \leq \frac{\min\{L_{ijkl}\}}{\kappa}\eta_W,$$

where, again, $\eta_W \ll 1$. Within the context of finite deformations and as elaborated upon in the next section, the parameter η_W should be typically chosen in the range $10^{-5} \leq \eta_W \leq 10^{-3}$.

Remark 7. *Equations (20)–(21) as a Ginzburg-Landau type model.* Instead of starting from the variational framework presented in Section 2, the governing equations (20) and (21) can be alternatively derived starting from a constitutive framework based on configurational forces (Gurtin, 1996; 2000). This alternative derivation will be presented elsewhere, but here we note that Eqs. (20)–(21) are of Ginzburg-Landau type, in particular, $(20)_1$ stands for the balance of Newtonian forces driving the deformation:

$$\text{Div}\,\mathbf{S} + \mathbf{b} = \mathbf{0},$$

while $(21)_{1-2}$ stand for the balance of configurational forces driving the phase transitions:

$$\left\{ \begin{array}{ll} \text{Div}\,\mathbf{C} + c_{\mathtt{i}} + c_{\mathtt{e}} = 0 & \text{if} \quad 0 < z < 1 \\ \text{Div}\,\mathbf{C} + c_{\mathtt{i}} + c_{\mathtt{e}} \geq (\text{ resp. } \leq)0 & \text{if} \quad z = 1(\text{ resp. } = 0) \end{array} \right. .$$

In the above expressions,

$$\mathbf{S}(\mathbf{X}, t) = (z^2 + \eta_W)\frac{\partial W}{\partial \mathbf{F}}(\nabla \mathbf{y}) + (z^2 + \eta_\kappa)\kappa\frac{\partial g}{\partial \mathbf{F}}(\nabla \mathbf{y})$$

denotes the first Piola-Kirchhoff stress tensor, conjugate to the deformation gradient $\mathbf{F}$, while

$$\left\{ \begin{array}{l} c_{\mathtt{i}}(\mathbf{X}, t) = -2z\left(W(\nabla \mathbf{y}) + \kappa g(\nabla \mathbf{y})\right) + \dfrac{3k(\dot{z}, \alpha, t^*)}{8\varepsilon} \\[2mm] \mathbf{C}(\mathbf{X}, t) = \dfrac{3}{4}\varepsilon k(\dot{z}, \alpha, t^*)\nabla z \end{array} \right.$$

denote the configurational *internal* force $c_{\mathtt{i}}$ and the configurational stress $\mathbf{C}$, conjugate to the configurational variables z and ∇z, at any material point $\mathbf{X} \in \Omega_0$ and time $t \in [0, T]$.

13

4. Numerical implementation

In this section, we present a finite-element scheme to generate numerical solutions for the coupled system of equations (20)–(21) in the context of $N = 2$ and 3 space dimensions; the case of $N = 1$ space dimension can be treated with simpler approaches which we do not discuss here. There are two major challenges in the construction of such a scheme. The first one is the selection of an appropriate finite-element discretization that is capable of dealing with large deformations and the near incompressibility typical of elastomers. The second one is the selection of an appropriate solver for the nonlinear algebraic equations resulting from the discretizations that is capable of dealing with the large changes in the deformation field $\mathbf{y}(\mathbf{X}, t)$ locally in space and time that can ensue from the nucleation of fracture. In order to resolve these challenges, as elaborated below, we base our proposed scheme on a non-conforming finite-element discretization of low order due to Crouzeix and Raviart (1973), suitably modified with a stabilization term (see, e.g., Babuska and Zlamal, 1973; Hansbo and Larson, 2003; Xu and Henao, 2011), and make use of an implicit gradient flow solver (see, e.g., Behrman, 1998; Neuberger, 2010) combined with a staggered strategy.

A few words about the organization of this section are in order. We begin in Subsection 4.1 by recasting the PDEs (20)–(21) into a weak form featuring admissible sets for the deformation field $\mathbf{y}(\mathbf{X}, t)$ and the phase field $z(\mathbf{X}, t)$ that are free of the constraints $\det \nabla \mathbf{y}(\mathbf{X}, t) > 0$ and $0 \leq z(\mathbf{X}, t) \leq 1$. In Subsection 4.2, we then consider a partition of the time interval under consideration $[0, T]$ into discrete times and spell out the corresponding time discretization of the governing PDEs in weak form. In Subsection 4.3, we further discretize in space the obtained set of time-discretized PDEs by means of a non-conforming finite element approximation. The last subsection elaborates on the solver utilized to generate numerical solutions for the set of nonlinear algebraic equations resulting from the discretizations.

4.1. Weak form of the governing equations

The inequalities $\det \nabla \mathbf{y}(\mathbf{X}, t) > 0$ and $0 \leq z(\mathbf{X}, t) \leq 1$ are difficult to enforce *a priori* when constructing numerical solutions for (20)–(21). Among several possible approaches, we choose to address this difficulty here by adopting a standard procedure followed in finite elasticity, namely, by suitably modifying the equations directly so that their solutions "always" satisfy the inequalities. Specifically, we restrict attention to stored-energy functions $W(\mathbf{F})$ with the property that

$$W(\mathbf{F}) \to \infty \quad \text{as} \quad \det \mathbf{F} \to 0+, \tag{23}$$

and add to the free-energy density $W_{\mathcal{S}}$ the penalty function

$$W_\nu(z) = \frac{\nu}{2} \left[(|z| - z)^2 + (|1 - z| - (1 - z))^2 \right], \tag{24}$$

where ν is a real-valued parameter (with unit $force/length^{N-1}$) to be selected so that $\nu \gg \max\{k(\dot{z}, \alpha, t^*)\}/\varepsilon$. Note that while the property (23) penalizes the violation of the inequality $\det \nabla \mathbf{y}(\mathbf{X}, t) > 0$, the addition of the function (24) to the free-energy density $W_{\mathcal{S}}$ penalizes the violation of the inequalities $0 \leq z(\mathbf{X}, t) \leq 1$. With the above modifications and upon the definition of the admissible sets

$$\mathcal{U} = \left\{ \mathbf{y} \in W^{1,p}(\Omega_0; \mathbb{R}^N) : \mathbf{y} = \boldsymbol{\xi} \text{ on } \partial\Omega_0^{\mathbf{y}} \right\}, \quad \mathcal{U}_0 = \left\{ \mathbf{y} \in W^{1,p}(\Omega_0; \mathbb{R}^N) : \mathbf{y} = \mathbf{0} \text{ on } \partial\Omega_0^{\mathbf{y}} \right\},$$

the coupled boundary-value problems (20)–(21) can be reformulated as the problem of finding the deformation field $\mathbf{y} \in \mathcal{U}$ and phase field $z \in W^{1,2}(\Omega_0)$ such that

$$\int_{\Omega_0} \left[(z^2 + \eta_W) \frac{\partial W}{\partial \mathbf{F}}(\nabla \mathbf{y}) + (z^2 + \eta_\kappa)\kappa \frac{\partial g}{\partial \mathbf{F}}(\nabla \mathbf{y}) \right] \cdot \nabla \mathbf{u} \, \mathrm{d}\mathbf{X} - \int_{\Omega_0} \mathbf{b} \cdot \mathbf{u} \, \mathrm{d}\mathbf{X} - \int_{\partial\Omega_0^{\mathbf{S}}} \boldsymbol{\sigma} \cdot \mathbf{u} \, \mathrm{d}\mathbf{X} = 0 \quad \forall \mathbf{u} \in \mathcal{U}_0, \, t \in [0, T] \tag{25}$$

and

$$\int_{\Omega_0} \left\{ \varepsilon k(\dot{z}, \alpha, t^*)\nabla z \cdot \nabla v + \left[\frac{8}{3} z \left(W(\nabla \mathbf{y}) + \kappa g(\nabla \mathbf{y}) \right) + 4\gamma \, z \, \frac{3^{\frac{p-4}{2}}}{|\nabla \mathbf{y}|^p} \left(\frac{\kappa}{\det \nabla \mathbf{y}} \nabla \mathbf{y} \cdot \frac{\partial g}{\partial \mathbf{F}}(\nabla \mathbf{y}) \right) - \frac{k(\dot{z}, \alpha, t^*)}{2\varepsilon} + \right. \right.$$
$$\left. \left. \frac{8}{3}\nu \left(2z - 1 + |1 - z| - |z| \right) \right] v \right\} \mathrm{d}\mathbf{X} = 0 \quad \forall v \in W^{1,2}(\Omega_0), \, t \in [0, T]. \tag{26}$$

14

where we note that the deformation field $\mathbf{y}(\mathbf{X}, t)$ is expected to belong to the Sobolev space $W^{1,p}(\Omega_0; \mathbb{R}^N)$ because of the growth condition (2) of the stored-energy function $W(\mathbf{F})$.

4.2. Time discretization

Consistent with the time discretization employed in Subsection 2.4, we consider next a partition of the time interval under consideration $[0, T]$ in the boundary-value problems (25)–(26) into discrete times $0 = t^0, t^1, ...t^m, t^{m+1}, ..., t^M = T$ together with the notation $\mathbf{y}^m(\mathbf{X}) = \mathbf{y}(\mathbf{X}, t^m)$, $z^m(\mathbf{X}) = z(\mathbf{X}, t^m)$, $\nabla \mathbf{y}^m(\mathbf{X}) = \nabla \mathbf{y}(\mathbf{X}, t^m)$, $\nabla z^m(\mathbf{X}) = \nabla z(\mathbf{X}, t^m)$, and $\alpha^m(\mathbf{X}) = \alpha(\mathbf{X}, t^m)$ for $m = 0, 1, 2, ..., M$. Making use of a first-order scheme, it then follows from the governing equations (25)–(26) that their solution for the fields $\mathbf{y}^{m+1} \in \mathcal{U}$ and $z^{m+1} \in W^{1,2}(\Omega_0)$ at time t^{m+1} is given in terms of their solution for the fields $\mathbf{y}^m \in \mathcal{U}$ and $z^m \in W^{1,2}(\Omega_0)$ at the previous time t^m, and the increments $\boldsymbol{\xi}^{m+1}(\mathbf{X}) = \boldsymbol{\xi}(\mathbf{X}, t^{m+1})$, $\boldsymbol{\sigma}^{m+1}(\mathbf{X}) = \boldsymbol{\sigma}(\mathbf{X}, t^{m+1})$, and $\mathbf{b}^{m+1}(\mathbf{X}) = \mathbf{b}(\mathbf{X}, t^{m+1})$ in the boundary data and body force, by the system of coupled boundary-value problems

$$
\int_{\Omega_0} \left[((z^{m+1})^2 + \eta_W) \frac{\partial W}{\partial \mathbf{F}}(\nabla \mathbf{y}^{m+1}) + ((z^{m+1})^2 + \eta_\kappa)\kappa \frac{\partial g}{\partial \mathbf{F}}(\nabla \mathbf{y}^{m+1}) \right] \cdot \nabla \mathbf{u} \, \mathrm{d}\mathbf{X} -
$$

$$
\int_{\Omega_0} \mathbf{b}^{m+1} \cdot \mathbf{u} \, \mathrm{d}\mathbf{X} - \int_{\partial \Omega_0^{\mathbf{S}}} \boldsymbol{\sigma}^{m+1} \cdot \mathbf{u} \, \mathrm{d}\mathbf{X} = 0 \qquad \forall \mathbf{u} \in \mathcal{U}_0 \tag{27}
$$

and

$$
\int_{\Omega_0} \left\{ \varepsilon k^{m+1} \nabla z^{m+1} \cdot \nabla v + \left[\frac{8}{3} z^{m+1} \left(W(\nabla \mathbf{y}^{m+1}) + \kappa g(\nabla \mathbf{y}^{m+1}) \right) + \right. \right.
$$

$$
4\gamma \, z^{m+1} \frac{3^{\frac{p-4}{2}}}{|\nabla \mathbf{y}^{m+1}|^p} \left(\frac{\kappa}{\det \nabla \mathbf{y}^{m+1}} \nabla \mathbf{y}^{m+1} \cdot \frac{\partial g}{\partial \mathbf{F}}(\nabla \mathbf{y}^{m+1}) \right) -
$$

$$
\left. \left. \frac{k^{m+1}}{2\varepsilon} + \frac{8}{3}\nu \left(2z^{m+1} - 1 + |1 - z^{m+1}| - |z^{m+1}| \right) \right] v \right\} \mathrm{d}\mathbf{X} = 0 \qquad \forall v \in W^{1,2}(\Omega_0), \tag{28}
$$

where, from the time discretizations of the toughness function (22) and memory quantities (19),

$$
k^{m+1} = \begin{cases} k_{\mathcal{S}}^0 + k_{\mathcal{F}}^0 + H_{\mathcal{S}}\left(\alpha^{m+1}(\mathbf{X})\right) + H_{\mathcal{F}}\left(\alpha^{m+1}(\mathbf{X})\right) & \text{if} \quad z^{m+1}(\mathbf{X}) - z^m(\mathbf{X}) \leq 0 \\[2mm] k_{\mathcal{S}}^0 - k_{\mathcal{H}}^0 + H_{\mathcal{S}}\left(\alpha^{m+1}(\mathbf{X})\right) - H_{\mathcal{H}}\left(\alpha^{m+1}(\mathbf{X})\right) & \text{if} \quad z^{m+1}(\mathbf{X}) - z^m(\mathbf{X}) > 0 \end{cases}
$$

with

$$
\alpha^{m+1}(\mathbf{X}) = \sum_{j=1}^{m^*} \left| z^j(\mathbf{X}) - z^{j-1}(\mathbf{X}) \right| \quad \text{and} \quad m^* = \max \left\{ j : j \in \{0, 1, 2, ..., m\} \text{ and } z^j(\mathbf{X}) = 1 \right\}.
$$

Notice that the above memory variable $\alpha^{m+1}(\mathbf{X})$ at time t^{m+1} depends on the history of the phase field $z(\mathbf{X}, t)$ only at most up to the time t^m (and *not* up to t^{m+1}), and hence it is a *constant* in the time-discretized equations (27)–(28).

4.3. Space discretization: non-conforming finite element approximation

Having reformulated the PDEs (20)–(21) into the time-discretized weak form (27)–(28), the next step is to further discretize these in space in order to be able to generate numerical solutions for the deformation field $\mathbf{y}^m(\mathbf{X})$ and the phase field $z^m(\mathbf{X})$ for all $\mathbf{X} \in \Omega_0$ at each of the discrete times $t^1, ...t^m, t^{m+1}, ..., t^M = T$ making up the time interval under consideration $[0, T]$; recall that at time $t^0 = 0$, these fields are known and given by $\mathbf{y}^0(\mathbf{X}) = \mathbf{X}$ and $z^0(\mathbf{X}) = z_0(\mathbf{X})$.

To this end, seeking the ability to discretize complex spatial domains in an expedient manner, we consider partitions ${}^h\Omega_0 = \bigcup_{e=1}^{N_e} \mathcal{E}^{(e)}$ with $\mathcal{E}^{(i)} \cap \mathcal{E}^{(j)} = \varnothing \; \forall i \neq j$ of the domain Ω_0 that comprise N_e non-overlapping simplicial elements $\mathcal{E}^{(e)}$; here, h stands for the diameter of the largest element. Specifically,

15

each element e possesses $N+1$ nodes with coordinates $\mathbf{X}^{(e,l)}$, $l = 1, ..., N+1$, located at the centroids of its $(N-1)$-dimensional faces. In terms of these nodal coordinates, with help of the reference simplicial element $\mathcal{T} = \left\{ \boldsymbol{\rho} : 0 \leq \rho_1, ..., \rho_N \leq 1, \sum_{l=1}^{N} \rho_l \leq 1 \right\}$, the domain occupied by each element e is defined parametrically by $\mathcal{E}^{(e)} = \left\{ \mathbf{X} : \sum_{l=1}^{N+1} N_{CR}^{(l)}(\boldsymbol{\rho}) \mathbf{X}^{(e,l)}, \boldsymbol{\rho} \in \mathcal{T} \right\}$. In this last expression, $N_{CR}^{(l)}(\boldsymbol{\rho})$ stand for the Crouzeix-Raviart *linear* shape functions $N_{CR}^{(1)}(\rho_1, \rho_2) = 1 - 2\rho_2$, $N_{CR}^{(2)}(\rho_1, \rho_2) = 2(\rho_1 + \rho_2) - 1$, $N_{CR}^{(3)}(\rho_1, \rho_2) = 1 - 2\rho_1$ for the case of $N = 2$ space dimensions, and $N_{CR}^{(1)}(\rho_1, \rho_2, \rho_3) = 1 - 3\rho_3$, $N_{CR}^{(2)}(\rho_1, \rho_2, \rho_3) = 3(\rho_1 + \rho_2 + \rho_3) - 1$, $N_{CR}^{(3)}(\rho_1, \rho_2, \rho_3) = 1 - 3\rho_1$, $N_{CR}^{(4)}(\rho_1, \rho_2, \rho_3) = 1 - 3\rho_2$ for the case of $N = 3$ space dimensions.

Given the above-described simplicial discretization in $N = 2$ and 3 space dimensions, we look for approximate solutions $^h\mathbf{y}^m(\mathbf{X})$ and $^h z^m(\mathbf{X})$ of the deformation field $\mathbf{y}^m(\mathbf{X})$ and the phase field $z^m(\mathbf{X})$ at time t^m in the Crouzeix-Raviart non-conforming finite-element spaces

$$^h\mathcal{U} = \{ {}^h\mathbf{y}^m : {}^h y_i^m(\mathbf{X})|_{\mathcal{E}^{(e)}} = \sum_{l=1}^{N+1} N_{CR}^{(l)}(\boldsymbol{\rho}) y_i^{m(e,l)}, \forall e = 1, ..., \mathbb{N}_e, \, {}^h\mathbf{y}^m \text{ is continuous on } \mathcal{C},$$

$$^h\mathbf{y}^m(\mathbf{X}^{(i)}) = \boldsymbol{\xi}^m(\mathbf{X}^{(i)}) \ \ \forall \mathbf{X}^{(i)} \in \mathcal{C} \cap \partial\Omega_0^{\mathbf{y}} \} \tag{29}$$

and

$$^h\mathcal{V} = \{ {}^h z^m : {}^h z^m(\mathbf{X})|_{\mathcal{E}^{(e)}} = \sum_{l=1}^{N+1} N_{CR}^{(l)}(\boldsymbol{\rho}) z^{m(e,l)}, \forall e = 1, ..., \mathbb{N}_e, \, {}^h z^m \text{ is continuous on } \mathcal{C} \}, \tag{30}$$

where $\mathcal{C}$ denotes the set of centroids of the $(N-1)$-dimensional faces in $^h\Omega_0$, while $y_i^{m(e,l)}$ and $z^{m(e,l)}$ denote the component i of the deformation field and the phase field at node l of element e at time t^m.

We remark that the class of non-conforming finite-element spaces (29) and (30) — along with corresponding non-conforming spaces of higher order — were originally introduced by Crouzeix and Raviart (1973) in the context of Stokes flow of incompressible viscous fluids under Dirichlet boundary conditions. Since then, they have been successfully utilized for a variety of other types of (linear and nonlinear) PDEs and boundary conditions (see, e.g., Falk, 1991; Burman and Hansbo, 2005; Rui and Zhang, 2009; Boffi et al., 2013), including those arising in the intimately related contexts of compressible finite elasticity (Xu and Henao, 2011) and of the regularized theory of fracture of Bourdin et al. (2008) at finite deformations (Henao et al., 2016). From a practical point of view, the alluring feature of non-conforming finite-element discretizations is that they may lead — sometimes, however, with the compulsory addition of stabilization terms (see, e.g., Falk, 1991) — to consistent and stable formulations with significantly fewer degrees of freedom than competing conforming dicretizations. This is indeed the case for the problem of interest here, where despite the low-order linear approximation of the finite-element spaces (29) and (30), with help of a suitable stabilization term to be described below, the resulting formulation can be shown (via numerical tests) to be stable and convergent irrespectively of the compressibility of the elastomer of interest.

Let us now denote by $\mathcal{I}$ the set of all internal $(N-1)$-dimensional faces in $^h\Omega_0$. Standard assembly procedures permit to construct global shape functions $^h N_{CR}^{(n)}(\mathbf{X})$, $n = 1, ..., \mathbb{N}_n$, so that for all $\mathbf{X} \in \left({}^h\Omega_0 \backslash \mathcal{I} \right) \cup \mathcal{C}$ the deformation trial field $^h\mathbf{y}^m(\mathbf{X})$ and the phase trial field $^h z^m(\mathbf{X})$ in (29) and (30) can be written in the global form

$$^h y_i^m(\mathbf{X}) = \sum_{n=1}^{\mathbb{N}_n} {}^h N_{CR}^{(n)}(\mathbf{X}) y_i^{m(n)} \quad \text{and} \quad {}^h z^m(\mathbf{X}) = \sum_{n=1}^{\mathbb{N}_n} {}^h N_{CR}^{(n)}(\mathbf{X}) z^{m(n)}, \tag{31}$$

where $\mathbb{N}_n$ stands for the total number of nodes in $^h\Omega_0$, while $y_i^{m(n)}$ and $z^{m(n)}$ correspond physically to the component i of the deformation field $^h\mathbf{y}^m(\mathbf{X})$ and the phase field $^h z^m(\mathbf{X})$ at node n and time t^m. We emphasize that the representations (31) apply *not* to all $\mathbf{X} \in {}^h\Omega_0$ but to $\mathbf{X} \in \left({}^h\Omega_0 \setminus \mathcal{I} \right) \cup \mathcal{C}$ given that the deformation and phase trial fields in the non-conforming finite-element spaces (29) and (30) are not necessarily bijective, and, in particular, can have discontinuities at $\mathbf{X} \in \mathcal{I} \setminus \mathcal{C}$. Indeed, for a given internal face $I \in \mathcal{I}$, denoting the two elements sharing that face by the 'left (L)' and the 'right (R)' elements and

16

their respective gather matrices[8] by $G_{ln}^{(L)}$ and $G_{ln}^{(R)}$, $l = 1, ..., N + 1$ and $n = 1, ..., \mathbb{N}_n$, the deformation and phase trial fields at $\mathbf{X} \in I$ are given by the two possibly distinct representations

$$
{}^h y_i^m(\mathbf{X}) = \begin{cases} \sum_{l=1}^{N+1} \sum_{n=1}^{\mathbb{N}_n} N_{CR}^{(l)}(\boldsymbol{\rho}) G_{ln}^{(L)} y_i^{m(n)} \\[2mm] \sum_{l=1}^{N+1} \sum_{n=1}^{\mathbb{N}_n} N_{CR}^{(l)}(\boldsymbol{\rho}) G_{ln}^{(R)} y_i^{m(n)} \end{cases} \quad \text{and} \quad {}^h z^m(\mathbf{X}) = \begin{cases} \sum_{l=1}^{N+1} \sum_{n=1}^{\mathbb{N}_n} N_{CR}^{(l)}(\boldsymbol{\rho}) G_{ln}^{(L)} z^{m(n)} \\[2mm] \sum_{l=1}^{N+1} \sum_{n=1}^{\mathbb{N}_n} N_{CR}^{(l)}(\boldsymbol{\rho}) G_{ln}^{(R)} z^{m(n)} \end{cases}
$$
(32)

in terms of the global degrees of freedom $y_i^{m(n)}$ and $z^{m(n)}$. Similarly, the corresponding approximations ${}^h\mathbf{u} \in {}^h\mathcal{U}_0 = \{{}^h\mathbf{y}^m : {}^h y_i^m(\mathbf{X})|_{\mathcal{E}^{(e)}} = \sum_{l=1}^{N+1} N_{CR}^{(l)}(\boldsymbol{\rho}) y_i^{m(e,l)}, \forall e = 1, ..., \mathbb{N}_e, \ {}^h\mathbf{y}^m$ is continuous on $\mathcal{C}$, ${}^h\mathbf{y}^m(\mathbf{X}^{(i)}) = 0 \ \forall \mathbf{X}^{(i)} \in \mathcal{C} \cap \partial\Omega_0^{\mathbf{y}}\}$ and $v \in {}^h\mathcal{V}$ of the test functions $\mathbf{u} \in \mathcal{U}_0$ and $v \in W^{1,2}(\Omega_0)$ admit the global representation

$$
{}^h u_i(\mathbf{X}) = \sum_n^{\mathbb{N}_n} {}^h N_{CR}^{(n)}(\mathbf{X}) u_i^{(n)} \quad \text{and} \quad {}^h v(\mathbf{X}) = \sum_n^{\mathbb{N}_n} {}^h N_{CR}^{(n)}(\mathbf{X}) v^{(n)}
$$
(33)

for $\mathbf{X} \in ({}^h\Omega_0 \setminus \mathcal{I}) \cup \mathcal{C}$ and

$$
{}^h u_i(\mathbf{X}) = \begin{cases} \sum_{l=1}^{N+1} \sum_{n=1}^{\mathbb{N}_n} N_{CR}^{(l)}(\boldsymbol{\rho}) G_{ln}^{(L)} u_i^{(n)} \\[2mm] \sum_{l=1}^{N+1} \sum_{n=1}^{\mathbb{N}_n} N_{CR}^{(l)}(\boldsymbol{\rho}) G_{ln}^{(R)} u_i^{(n)} \end{cases} \quad \text{and} \quad {}^h v(\mathbf{X}) = \begin{cases} \sum_{l=1}^{N+1} \sum_{n=1}^{\mathbb{N}_n} N_{CR}^{(l)}(\boldsymbol{\rho}) G_{ln}^{(L)} v^{(n)} \\[2mm] \sum_{l=1}^{N+1} \sum_{n=1}^{\mathbb{N}_n} N_{CR}^{(l)}(\boldsymbol{\rho}) G_{ln}^{(R)} v^{(n)} \end{cases}
$$
(34)

for $\mathbf{X}$ in any of the internal faces I in the set $\mathcal{I}$.

Direct substitution of the representations (31)–(34) in the PDEs (27) and (28), together with use of the notation $\mathbb{N} = \{n : \mathbf{X}^{(n)} \in {}^h\Omega_0\}$ and $\mathbb{Y} = \{n : \mathbf{X}^{(n)} \in {}^h\Omega_0 \cap \partial\Omega_0^{\mathbf{y}}\}$ for the sets of all node numbers $\mathbb{N}$ and of boundary-node numbers $\mathbb{Y}$ where deformations are applied, and the addition of the stabilization term

$$
\sum_{I \in \mathcal{I}} \frac{q}{h_I} \int_I [\![{}^h\mathbf{y}^{m+1}]\!] \cdot [\![{}^h\mathbf{u}]\!] \, d\mathbf{X}
$$
(35)

to the PDE (27), leads finally to the following system of coupled nonlinear algebraic equations

$$
\begin{aligned}
\mathcal{G}_1({}^h\mathbf{y}^{m+1}, {}^h z^{m+1}) &\doteq \int_{\Omega_0} \left[(({}^h z^{m+1})^2 + \eta_W) \frac{\partial W}{\partial F_{ij}}(\nabla^h\mathbf{y}^{m+1}) + (({}^h z^{m+1})^2 + \eta_\kappa) \kappa \frac{\partial g}{\partial F_{ij}}(\nabla^h\mathbf{y}^{m+1}) \right] \frac{\partial^h N_{CR}^{(n)}}{\partial X_j}(\mathbf{X}) d\mathbf{X} - \\
&\quad \int_{\Omega_0} b_i^{m+1} \, {}^h N_{CR}^{(n)}(\mathbf{X}) \, d\mathbf{X} - \int_{\partial\Omega_0^{\mathbf{s}}} \sigma_i^{m+1} \, {}^h N_{CR}^{(n)}(\mathbf{X}) \, d\mathbf{X} + \\
&\quad \sum_{I \in \mathcal{I}} \frac{q}{h_I} \int_I \left(\sum_{l=1}^{N+1} \sum_{n=1}^{N_n} (G_{ln}^{(L)} - G_{ln}^{(R)}) N_{CR}^{(l)}(\boldsymbol{\rho}) y_i^{m+1(n)} \right) \left(\sum_{l=1}^{N+1} (G_{ln}^{(L)} - G_{ln}^{(R)}) N_{CR}^{(l)}(\boldsymbol{\rho}) \right) d\mathbf{X} = 0, \quad n \in \mathbb{N} \setminus \mathbb{Y},
\end{aligned}
$$
(36)

and

$$
\begin{aligned}
\mathcal{G}_2({}^h\mathbf{y}^{m+1}, {}^h z^{m+1}) &\doteq \int_{\Omega_0} \left\{ \varepsilon \, {}^h k^{m+1} \nabla^h z_i^{m+1} \frac{\partial^h N_{CR}^{(n)}}{\partial X_i}(\mathbf{X}) + \left[\frac{8}{3} \, {}^h z^{m+1} \left(W(\nabla^h\mathbf{y}^{m+1}) + \kappa g(\nabla^h\mathbf{y}^{m+1}) \right) + \right. \right. \\
&\quad 4\gamma \, {}^h z^{m+1} \frac{3^{\frac{p-4}{2}}}{|\nabla^h\mathbf{y}^{m+1}|^p} \left(\frac{\kappa}{\det \nabla^h\mathbf{y}^{m+1}} \nabla^h\mathbf{y}^{m+1} \cdot \frac{\partial g}{\partial \mathbf{F}}(\nabla^h\mathbf{y}^{m+1}) \right) - \frac{{}^h k^{m+1}}{2\varepsilon} + \\
&\quad \left. \left. \frac{8}{3} \nu \left(2 \, {}^h z^{m+1} - 1 + |1 - {}^h z^{m+1}| - |{}^h z^{m+1}| \right) \right] \, {}^h N_{CR}^{(n)}(\mathbf{X}) \right\} d\mathbf{X} = 0, \quad n \in \mathbb{N},
\end{aligned}
$$
(37)

---

[8] The definition of the gather matrices $G_{ln}^{(e)}$ ($e = 1, ..., \mathbb{N}_e$) adopted here is such that $y_i^{m(e,l)} = \sum_{n=1}^{\mathbb{N}_n} G_{ln}^{(e)} y_i^{m(n)}$ and $z^{m(e,l)} = \sum_{n=1}^{\mathbb{N}_n} G_{ln}^{(e)} z^{m(n)}$.

where

$$
{}^h k^{m+1} = \begin{cases} k_{\mathcal{S}}^0 + k_{\mathcal{F}}^0 + H_{\mathcal{S}}\left({}^h\alpha^{m+1}(\mathbf{X})\right) + H_{\mathcal{F}}\left({}^h\alpha^{m+1}(\mathbf{X})\right) & \text{if} \quad {}^h z^{m+1}(\mathbf{X}) - {}^h z^m(\mathbf{X}) \leq 0 \\[2mm] k_{\mathcal{S}}^0 - k_{\mathcal{H}}^0 + H_{\mathcal{S}}\left({}^h\alpha^{m+1}(\mathbf{X})\right) - H_{\mathcal{H}}\left({}^h\alpha^{m+1}(\mathbf{X})\right) & \text{if} \quad {}^h z^{m+1}(\mathbf{X}) - {}^h z^m(\mathbf{X}) > 0 \end{cases} \tag{38}
$$

with

$$
{}^h\alpha^{m+1}(\mathbf{X}) = \sum_{j=1}^{m^*} \left| {}^h z^j(\mathbf{X}) - {}^h z^{j-1}(\mathbf{X}) \right| \quad \text{and} \quad m^* = \max\left\{ j : j \in \{0, 1, 2, ..., m\} \text{ and } {}^h z^j(\mathbf{X}) = 1 \right\},
$$

for the global degrees of freedom $y_i^{m+1(n)}$ and $z^{m+1(n)}$ that define, via expressions (31), the deformation field ${}^h\mathbf{y}^{m+1}(\mathbf{X})$ and the phase field ${}^h z^{m+1}(\mathbf{X})$ for all $\mathbf{X} \in \Omega_0$ at time t^{m+1}.

We conclude this subsection by remarking that the addition of a stabilization term to the discretized PDE (36) is essential to avoid spurious rigid body rotations when dealing with pure traction or mixed boundary conditions; see Falk (1991) for a thorough study of this issue in the simpler context of linear elasticity. By contrast, the discretized PDE (37) does not require of any stabilization term, irrespectively of the applied boundary conditions. The specific stabilization term (35) that we employ here — which penalizes the jump of the deformation field across element faces and where h_I stands for the diameter of the internal face I in the set $\mathcal{I}$, $[\![\cdot]\!]$ denotes the jump of a given quantity across the corresponding internal face, and q is a stabilization parameter (with unit $force/length^{N-1}$) whose selection is described below — was chosen based on its performance over a wide range of numerical tests involving various specimen geometries and boundary conditions.

4.4. The solver: staggered scheme and implicit gradient flow

Having discretized the governing PDEs (20)–(21) into the system of coupled nonlinear algebraic equations (36)–(37) for the global degrees of freedom $y_i^{m+1(n)}$ and $z^{m+1(n)}$ at time t^{m+1}, the final step is to solve these for a given time discretization $0 = t^0, t^1, ... t^m, t^{m+1}, ..., t^M = T$, given space discretization ${}^h\Omega_0$, given stored-energy functions $W(\mathbf{F})$, $g(\mathbf{F})$, and compressibility parameter κ, given toughness function $k(\dot{z}, \alpha, t^*)$, and given applied boundary data $\boldsymbol{\xi}(\mathbf{X}, t)$, $\boldsymbol{\sigma}(\mathbf{X}, t)$, and body force $\mathbf{b}(\mathbf{X}, t)$. Consistent with the approach outlined in Subsection 2.4, we do so by following a staggered scheme[9], which involves solving the equations (36) and (37) iteratively one after the other at every time step t^m until convergence is reached. Specifically, the algorithm to solve (36) and (37) for $y_i^{m+1(n)}$ and $z^{m+1(n)}$ at t^{m+1} is as follows:

- *Step 0.* Set $r = 1$ and define appropriate tolerances $TOL_1, TOL_2 > 0$ and maximum number of iterations $\mathtt{I}_1$. For a given solution ${}^h\mathbf{y}^m$ and ${}^h z^m$ at time t^m, define also ${}^h\mathbf{y}^{m+1,0} = {}^h\mathbf{y}^m$ and ${}^h z^{m+1,0} = {}^h z^m$.

- *Step 1.* Given the increments $\boldsymbol{\xi}^{m+1}(\mathbf{X})$, $\boldsymbol{\sigma}^{m+1}(\mathbf{X})$, and $\mathbf{b}^{m+1}(\mathbf{X})$ in boundary data and body force, find ${}^h\mathbf{y}^{m+1,r} \in {}^h\mathcal{U}$ such that

$$
\mathcal{G}_1({}^h\mathbf{y}^{m+1,r}, {}^h z^{m+1,r-1}) = 0. \tag{39}
$$

- *Step 2.* Having solved the sub-problem (39) for ${}^h\mathbf{y}^{m+1,r}$, find ${}^h z^{m+1,r} \in {}^h\mathcal{V}$ such that

$$
\mathcal{G}_2({}^h\mathbf{y}^{m+1,r}, {}^h z^{m+1,r}) = 0. \tag{40}
$$

---

[9]Standard monolithic schemes are doomed to fail because of the very different physical nature of the discretized PDEs (36) and (37); see, however, the work of Gerasimov and De Lorenzis (2016) for some possible modifications of monolithic schemes that may prove viable.

- *Step 3.* If $\| \mathcal{G}_1({}^h\mathbf{y}_j^{m+1,r}, {}^hz^{m+1,r}) \| / \| \mathcal{G}_1({}^h\mathbf{y}_j^{m+1,0}, {}^hz^{m+1,0}) \| \leq TOL_1$ and $\| \mathcal{G}_2({}^h\mathbf{y}_j^{m+1,r}, {}^hz^{m+1,r}) \| / \| \mathcal{G}_2({}^h\mathbf{y}_j^{m+1,1}, {}^hz^{m+1,0}) \| \leq TOL_2$ or $r > \mathtt{I}_1$, then set ${}^h\mathbf{y}^{m+1} = {}^h\mathbf{y}^{m+1,r}$, ${}^hz^{m+1} = {}^hz^{m+1,r}$, and move to the next time step t^{m+2}; otherwise set $r \leftarrow r + 1$ and go back to Step 1.

In all of the numerical results that are presented in the sequel, we have made use of the tolerance values $TOL_1 = TOL_2 = 10^{-6}$ and a maximum number of iterations of $\mathtt{I}_1 = 40$. In regard to these choices, we remark that numerical tests have indicated that equations (39) and (40) may not be satisfied up to the above-specified tolerances after 40 iterations, instead, many more iterations (in the order of several hundreds) might be required. The tests have also indicated, however, that increasing the number of iterations beyond 40 does not significantly change the obtained solution for ${}^h\mathbf{y}^{m+1}$ and ${}^hz^{m+1}$, thus our choice of $\mathtt{I}_1 = 40$ to reduce computational cost. We now describe the methods of solution for each of the sub-problems (39) and (40) ensuing from the proposed staggered scheme.

The sub-problem (39). We begin by remarking that the sub-problem (39), in view of the fact that the discretized phase field ${}^hz^{m+1,r-1}$ is kept fixed, is essentially nothing more than a finite elasticity problem. While Newton's method, or any of its variants (see, in particular, Farrell and Maurini, 2017), can be successfully utilized to generate solutions of (39) for a variety of cases, it does not seem capable of delivering converged solutions for general specimen geometries and loading conditions. This is because in the context of finite deformations of interest here (as opposed to the classical context of small-strain linear elasticity), the nucleation of fracture at a material point can lead to sudden large changes in the deformation field in the neighborhood of that point. Motivated by the work of Henao et al. (2016) on similar types of PDEs, we address this issue by employing an implicit gradient flow method of solution; the interested reader is referred to Behrman (1998) and Neuberger (2010) for an overview of gradient flow methods including a brief historical account tracing its origins back to the pioneering work of Cauchy (1847).

The basic idea behind the gradient flow method that we adopt here is to identify the solution ${}^h\mathbf{y}^{m+1,r}$ of the sub-problem (39) with the $\lim_{s \to +\infty} {}^h\mathbf{y}^{m+1,r}(s)$, where the function ${}^h\mathbf{y}^{m+1,r}(s) \in {}^h\mathcal{U}$ is implicitly defined by the system of first-order nonlinear ordinary differential equations (ODEs)

$$\int_{\Omega_0} \frac{\partial}{\partial X_j}\left(\frac{\mathrm{d}\,{}^h\mathbf{y}^{m+1,r}}{\mathrm{d}s}(s)\right) \frac{\partial {}^hN_{CR}^{(n)}}{\partial X_j}(\mathbf{X})\,\mathrm{d}\mathbf{X} = -\mathcal{G}_1({}^h\mathbf{y}^{m+1,r}(s), {}^hz^{m+1,r-1}) \tag{41}$$

subject to the initial condition

$$ {}^h\mathbf{y}^{m+1,r}(0) = {}^h\mathbf{y}^{m+1,r-1}. \tag{42}$$

In practice, the solution to this system of ODEs, which can be constructed numerically with a plethora of schemes, converges to the solution of (39), up to a given tolerance, for a finite value of the parametric variable s. Here, we make use of a first-order scheme to solve (41)–(42). Specifically, the algorithm to find the solution of (39) through solving (41)–(42) for ${}^h\mathbf{y}^{m+1,r}(s)$ is as follows:

- *Step 0.* Set $j = 1$ and define an appropriate tolerance TOL_3 and maximum number of iterations $\mathtt{I}_2$. Define also ${}^h\mathbf{y}_0^{m+1,r} = {}^h\mathbf{y}^{m+1,r}(0) = {}^h\mathbf{y}^{m+1,r-1}$.

- *Step 1.* Choose an appropriate parametric step $\Delta s_j^{m+1,r}$ and solve the following system of *linear* algebraic equations for ${}^h\delta\mathbf{y}_j^{m+1,r} \in {}^h\mathcal{U}_0$:

$$g({}^h\delta\mathbf{y}_j^{m+1,r}) + \Delta s_j^{m+1,r}\,D\mathcal{G}_1({}^h\mathbf{y}_{j-1}^{m+1,r}, {}^hz^{m+1,r-1}; {}^h\delta\mathbf{y}_j^{m+1,r}) = -\Delta s_j^{m+1,r}\,\mathcal{G}_1({}^h\mathbf{y}_{j-1}^{m+1,r}, {}^hz^{m+1,r}), \tag{43}$$

where $g({}^h\delta\mathbf{y}_j^{m+1,r}) = \int_{\Omega_0}(\partial\,{}^h\delta\mathbf{y}_j^{m+1,r}(s)/\partial X_j)\,(\partial\,{}^hN_{CR}^{(n)}/\partial X_j)\,\mathrm{d}\mathbf{X}$ and $D\mathcal{G}_1({}^h\mathbf{y}_{j-1}^{m+1,r}, {}^hz^{m+1,r-1}; {}^h\delta\mathbf{y}_j^{m+1,r})$ stands for the Gâteaux derivative of $\mathcal{G}_1$ at $\mathbf{y}_{j-1}^{m+1,r} \in {}^h\mathcal{U}$ in the direction $\delta\mathbf{y}_j^{m+1,r} \in {}^h\mathcal{U}_0$. Having solved (43) for ${}^h\delta\mathbf{y}_j^{m+1,r}$, set ${}^h\mathbf{y}_j^{m+1,r} = {}^h\mathbf{y}_{j-1}^{m+1,r} + {}^h\delta\mathbf{y}_j^{m+1,r}$.

- *Step 2.* If $\parallel \mathcal{G}_1({}^h\mathbf{y}_j^{m+1,r}, {}^h z^{m+1,r}) \parallel / \parallel \mathcal{G}_1({}^h\mathbf{y}_0^{m+1,r}, {}^h z^{m+1,r}) \parallel < TOL_3$ or $j > \mathtt{I}_2$, then set ${}^h\mathbf{y}^{m+1,r} = {}^h\mathbf{y}_j^{m+1,r}$ and exit; otherwise set $j \leftarrow j+1$ and go back to Step 1.

In all of the numerical results that are presented in the sequel, we have made use of the tolerance value $TOL_3 = 10^{-10}$ and a maximum number of iterations of $\mathtt{I}_2 = 50$. Numerical tests have indicated that if the increment $\Delta s_j^{m+1,r}$ in Step 1 is chosen appropriately, then the algorithm converges well within 50 iterations, save for when the solution experiences sudden large changes. In this regard, we remark that the algorithm converges linearly when $\Delta s_j^{m+1,r}$ is sufficiently small, while it can converge quadratically when $\Delta s_j^{m+1,r}$ is large. Indeed, when the solution changes smoothly, $\Delta s_j^{m+1,r}$ can be taken to be a large number and the algorithm will converge quadratically much like Newton's method. On the other hand, when the solution experiences sudden large changes, $\Delta s_j^{m+1,r}$ needs to be reduced to maintain convergence, in which case the rate of convergence is only linear.

The sub-problem (40). Turning our attention now to the sub-problem (40), we begin by recognizing that, except for the dependence of the toughness function ${}^h k^{m+1}$ on the unknown ${}^h z^{m+1}(\mathbf{X})$ itself through the sign of the incremental term ${}^h z^{m+1}(\mathbf{X}) - {}^h z^m(\mathbf{X})$, this problem is essentially nothing more than a standard elliptic problem for a scalar-valued field. As opposed to the sub-problem (39), the sub-problem (40) can be solved with the standard Newton's method. To do so efficiently, however, one must devise a scheme that chooses efficiently the correct branch in (38) for ${}^h k^{m+1}$. Numerical experiments have indicated that the sign of ${}^h z^{m+1}(\mathbf{X}) - {}^h z^m(\mathbf{X})$ can be determined *a priori* from the corresponding incremental change in the value of the elastic energy, that is, the quantity $W\left(\nabla^h \mathbf{y}^{m+1}\right) + \kappa g\left(\nabla^h \mathbf{y}^{m+1}\right) - W\left(\nabla^h \mathbf{y}^m\right) - \kappa g\left(\nabla^h \mathbf{y}^m\right)$, which happens to be known while solving sub-problem (40) due to the staggered nature of our scheme. In particular, consistent with physical expectations, if the elastic energy increases (decreases) at a given material point while going from t^m to t^{m+1}, the phase field, if it evolves, can only decrease (increase) so that ${}^h z^{m+1}(\mathbf{X}) - {}^h z^m(\mathbf{X}) \le 0$ $\left({}^h z^{m+1}(\mathbf{X}) - {}^h z^m(\mathbf{X}) > 0\right)$. Accordingly, in our scheme, we use the change in the value $W\left(\nabla^h \mathbf{y}^{m+1}\right) + \kappa g\left(\nabla^h \mathbf{y}^{m+1}\right) - W\left(\nabla^h \mathbf{y}^m\right) - \kappa g\left(\nabla^h \mathbf{y}^m\right)$ to select the appropriate branch for the toughness function ${}^h k^{m+1}$ in solving problem (40).

We close this section by recording a few additional remarks regarding the above-laid-out numerical implementation. Within the context of finite deformations of interest here, numerical experiments have indicated that the parameter η_W should be typically chosen to be in the range $\eta_W \in [10^{-5}, 10^{-3}]$; see Remark 6 for the corresponding choice for the parameter η_κ. They have also indicated that it suffices to select the parameter ν in (24) to be from 10 to 100 times larger than $\max\{k(\dot{z}, \alpha, t^*)\}/\varepsilon$. The selection of the value for the penalty parameter q in (35) is more subtle. Its optimal value appears to depend on the specifics of the boundary-value problem being solved, in particular, on the compressibility of the elastomer. In general, however, our numerical tests for the prominent case of isotropic elastomers have shown that choosing q to be of the order of the initial shear modulus of the elastomer under consideration typically renders an optimally convergent formulation. We also emphasize that the spatial discretization should be done so that the mesh is uniform (unless, of course, if one has prior knowledge of where the nucleation and propagation of fracture and healing will take place) and unstructured to prevent mesh-induced preference for nucleation and propagation of fracture and healing (see, e.g., Negri, 1999; 2003). Furthermore, in general, it suffices to select a mesh size such that $h = \varepsilon/3$.

5. Numerical assessment through benchmark simulations

Next, we demonstrate the accuracy and stability of the proposed numerical scheme. To that end, we carry out simulations of two benchmark problems: (*i*) the L-shaped concrete panel problem, and (*ii*) the problem of a plane-strain crack embedded in a slab of rubber under tension. Both simulations are run in plane strain within a three dimensional setting and compared with the simulations in Mesgarnejad et al. (2015) for the L-shaped panel problem and those in Miehe and Schänzel (2014) for the plane-strain crack problem.

5.1. The L-shaped concrete panel problem

The specimen geometry and applied boundary conditions for this problem, the genesis of which can be traced back to Winkler (2001), are schematically depicted in Fig. 2(a). The specimen is isotropic, linear elastic with shear modulus $\mu = 10.95\,\text{GPa}$, Lamé constant $\Lambda = 6.16\,\text{GPa}$, and has a critical energy release rate of $G_c = 95\,\text{J/m}^2$.

In our simulation, we identify the compressibility parameter κ with the Lamé constant Λ and take the stored-energy functions $W(\mathbf{F})$ and $g(\mathbf{F})$ characterizing the finite elasticity of the material to be given by

$$W(\mathbf{F}) = \frac{\mu}{2}\left(\mathbf{F}\cdot\mathbf{F} - 3\right) - \mu\ln\left(\det\mathbf{F}\right) \qquad \text{and} \qquad g(\mathbf{F}) = \frac{1}{2}\left(\det\mathbf{F} - 1\right)^2.$$

This choice of functions linearizes properly in the limit of small deformations (as $\mathbf{F}\to\mathbf{I}$) in the sense that the resulting material is an isotropic linearly elastic solid with shear modulus $\mu = 10.95\,\text{GPa}$ and Lamé constant $\kappa = \Lambda$, as required. Moreover, for direct comparison with the results of Mesgarnejad et al. (2015), we take $\mathbf{b}(\mathbf{X},t) = \mathbf{0}$ in (20) and $k_\mathcal{S} = k_\mathcal{H} = 0$, $k_\mathcal{F} = G_c = 95\,\text{J/m}^2$ in (21). In other words, there are no body forces, the nucleation and propagation of fracture is taken to be purely dissipative, so that in particular healing is prohibited, and the fracture toughness is a constant. Furthermore, since the material is highly compressible, we take $\gamma = 0$ and $\eta_W = \eta_\kappa = 10^{-7}$. As in Mesgarnejad et al. (2015), we set the value of the parameter ε at 3.125 mm and fix the phase field z at 1 in the areas depicted in gray in Fig. 2(a) and at 0 along the corner where the nucleation of fracture is expected. We employ a uniform mesh of size $h = \varepsilon/5 = 0.625$ mm throughout the central region of the specimen, and a coarser mesh elsewhere.
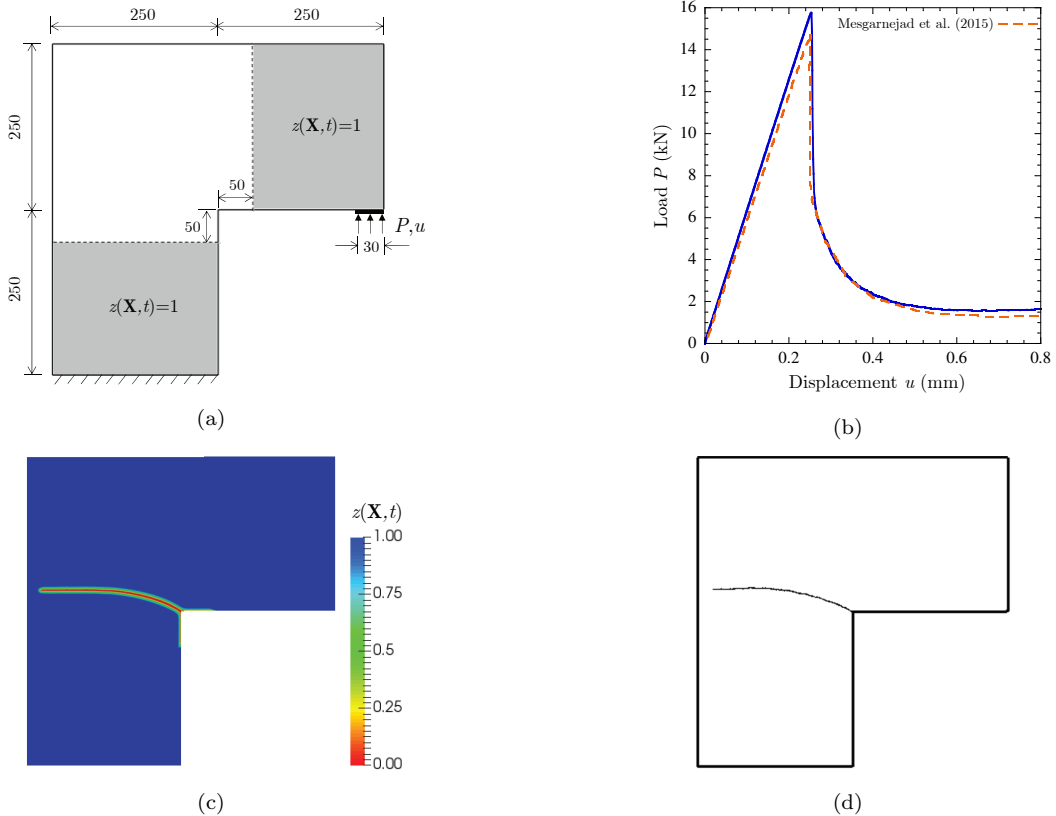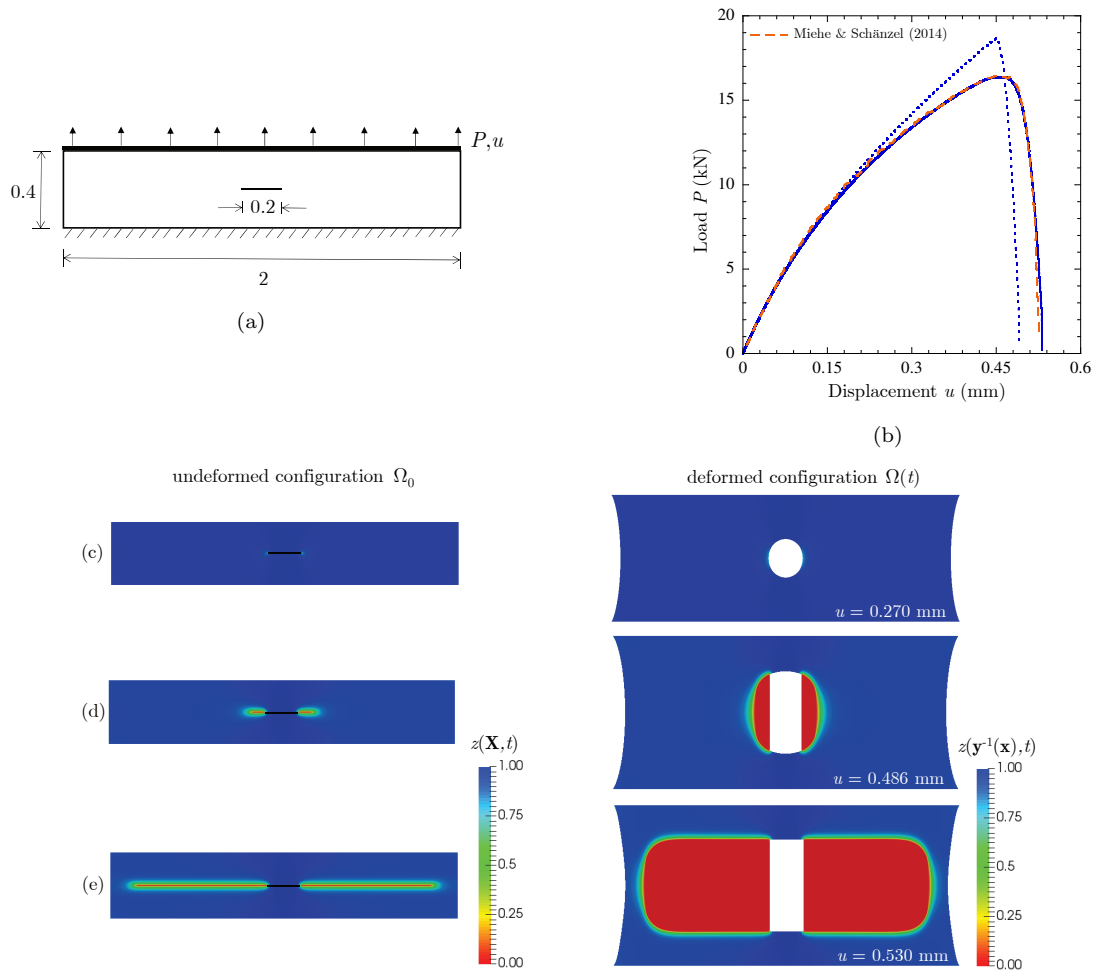

Figure 2: (a) Schematics of the initial specimen geometry (all sizes are in mm) and applied boundary conditions for the L-shaped concrete panel problem. (b) Plot (solid line) of the computed load P as a function of the applied displacement u compared with the corresponding result (dashed line) in Mesgarnejad et al. (2015). (c) Contour plot of the phase field at the applied displacement $u = 0.8$ mm. (d) The crack path obtained in Mesgarnejad et al. (2015) at $u = 0.8$ mm.

21

The plots presented in Fig. 2(b) show that the load-displacement (P vs. u) response computed from our simulation (solid line) is in good agreement with the corresponding result (dashed line) of Mesgarnejad et al. (2015) over the entire loading process; the small differences between the two results might be due to the fact that our simulation is for finite deformations, as opposed to small-strain linear elasticity. Moreover, the crack path predicted by our simulation, shown in Fig. 2(c), is also in good agreement with that obtained there and shown in Fig. 2(d). In particular, we remark that the initial crack angle predicted by our simulation, 25.17°, agrees approximately with that reported in Mesgarnejad et al. (2015), namely, 26.06°.

5.2. A plane-strain crack embedded in a slab of rubber under tension

For comparison with the results of Miehe and Schänzel (2014), the specimen geometry and applied boundary conditions that we select for this benchmark problem are those schematically depicted in Fig.

Figure 3: (a) Schematics of the initial specimen geometry (all sizes in mm) and applied boundary conditions for the problem of a plane-strain crack embedded in a slab of rubber under tension. (b) Plots (dotted and solid lines) of the computed load P as a function of the applied displacement u compared with the corresponding result (dashed line) of Miehe and Schänzel (2014). (c)–(e) Contour plots of the phase field in the undeformed and the deformed configurations at three different values of the applied displacement u: (c) immediately before the crack starts to propagate ($u = 0.270$mm), (d) after the crack has started to propagate ($u = 0.486$mm), and (e) near complete rupture of the specimen ($u = 0.530$mm).

3(a). The isotropic nonlinear elastic behavior of the specimen is characterized by the stored-energy functions

$$W(\mathbf{F}) = \frac{\mu}{2}\left(\mathbf{F}\cdot\mathbf{F} - 3\right) + \frac{\mu^2}{\Lambda}\left(\left(\det\mathbf{F}\right)^{-\Lambda/\mu} - 1\right) \qquad \text{and} \qquad g(\mathbf{F}) = 0$$

with material parameters $\mu = 5$ MPa and $\Lambda = 7.50$ MPa.[10] As in the previous simulation, we also take $\mathbf{b}(\mathbf{X},t) = \mathbf{0}$ in (20) and $k_{\mathcal{S}} = k_{\mathcal{H}} = 0$, $k_{\mathcal{F}} = 2.4 \times 10^3$ J/m^2 in (21). Moreover, we take $\varepsilon = 0.01$ mm, $\eta_W = 10^{-5}$, and use a uniform fine mesh of size $h = \varepsilon/10 = 1$ μm throughout the mid-plane region of the slab where the crack is expected to propagate. Note that we do not need to prescribe values for the parameters γ and η_κ here since the material is inherently compressible with $g(\mathbf{F}) = 0$.

Figure 3(b) presents the comparison of the load-displacement (P vs. u) response computed from our simulation (dotted line) with the result (dashed line) in Miehe and Schänzel (2014). The regularization of surface area in that work is different from the one that we have used.[11] For a more direct comparison, we have also carried out the simulation with their regularization and included the result (solid line) in Fig. 3(b). We observe that this second result is in good agreement with that reported there over the entire loading process. We note as well that the choice of the regularized area functional impacts the result, especially as far as the value of the force at which the crack starts to propagate is concerned; see, e.g., Pham et al. (2011) for an in-depth discussion of this issue in the context of damage models. For completeness, we illustrate in Figs. 3(c)–(e) contour plots of the phase-field variable in the undeformed and the deformed configurations at three different values of the applied displacement $u = 0.270, 0.486$, and 0.530 mm.

6. Sample simulations of the Gent-Park experiment

In this section, we explore the capabilities of the proposed theory to describe the nucleation and propagation of fracture and healing in elastomers via sample simulations of the Gent-Park experiment schematically depicted in Fig. 4. For computational frugality, the simulations are carried out in the context of $N = 2$ space dimensions corresponding to conditions of plane strain in a three dimensional setting.
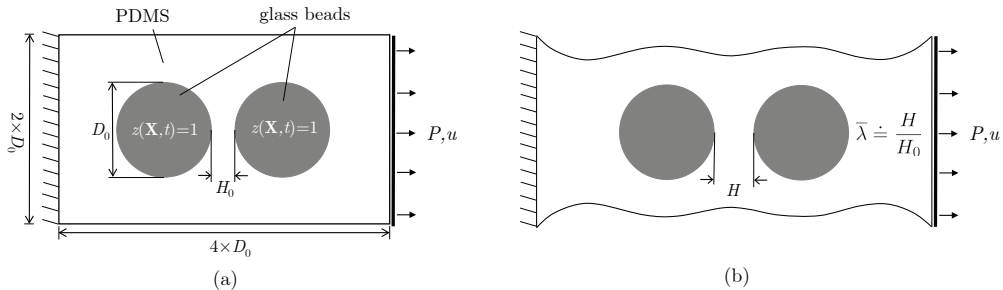

Figure 4: Schematics of the specimen geometry, in (a) its initial configuration at time $t = 0$ and in (b) a deformed configuration at a later time $t > 0$, and the applied boundary conditions used in the simulations of the Gent-Park experiment. The ratio $\bar{\lambda} \doteq H/H_0$ identified in part (b) provides an expedient average measure of the stretch across the gap between the beads.

For later comparison with the experiments of Poulain et al. (2017), we shall consider the diameter D_0 of the firmly embedded glass beads to be of the order of millimeters, the gap H_0 between the beads to be sub-millimetric, and shall take the stored-energy functions characterizing the nonlinear elastic behavior of the embedding elastomer to be given by

$$W(\mathbf{F}) = \sum_{r=1}^{2} \frac{3^{1-\beta_r}}{2\beta_r}\mu_r\left[(\mathbf{F}\cdot\mathbf{F})^{\beta_r} - 3^{\beta_r}\right] - \sum_{r=1}^{2}\mu_r \ln\left(\det\mathbf{F}\right) \quad \text{and} \quad g(\mathbf{F}) = \frac{1}{2}\left(\det\mathbf{F} - 1\right)^2 \qquad (44)$$

---

[10]There is an apparent discrepancy between the value of Λ reported in Miehe and Schänzel (2014) and the value that is actually used in the reported simulations, namely, $\Lambda = 7.50$ MPa.

[11]In Miehe and Schänzel (2014), the more conventional regularized functional form $\mathcal{S}_\varepsilon(z) = 1/2((1-z)^2/\varepsilon + \varepsilon\nabla z\cdot\nabla z)$ is being used.

with the set of material parameters given in Table 1. This choice describes accurately the nonlinear elastic behavior of a PDMS grade — that corresponding to a 45:1 ratio of base to curing agent — used in Poulain et al. (2017). Moreover, we take the elastic behavior of the beads[12] to be characterized as well by (44), but with different material parameters, as indicated in Table 1. This choice also describes accurately the mechanical behavior of the glass beads used in the experiments of Poulain et al. (2017). In particular, notice that the initial shear modulus of the beads, given by the combination $\mu_1 + \mu_2 = 10$ GPa, is more than four orders of magnitude larger than that of the PDMS and so, much like in the experiments, they effectively behave as rigid domains in the simulations. Contrary to its nonlinear elastic properties, there is no direct experimental knowledge of the fracture and healing properties of the PDMS 45:1. Accordingly, in the simulations that follow, we shall consider toughness functions $k(\dot{z}, \alpha, t^*)$ spanning over a wide range of physically plausible properties, as well as a range of parameters γ=ly, in all the simulations reported below, $\mathbf{b}(\mathbf{X}, t) = \mathbf{0}$, $\varepsilon = 5$ μm, $\eta_W = 10^{-3}$, $\eta_\kappa = 10^{-6}$, $\nu = 10^2 \max\{k(\dot{z}, \alpha, t^*)\}/\varepsilon$, the mesh is uniform of size $h = \varepsilon/3 = 1.67$ μm in the PDMS region between the beads, and $z(\mathbf{X}, t)$ is set at 1 inside the beads (since these do not fracture).

Table 1: Material parameters in the stored-energy function $(44)_1$ and the compressibility parameter κ characterizing the nonlinear elastic behavior of the PDMS and the glass beads used in the simulations of the Gent-Park experiment in Fig. 4.

	β_1	β_2	μ_1 (MPa)	μ_2 (MPa)	κ (MPa)
PDMS 45:1	-1.10010	1.45673	0.00522	0.00955	$10^3(\mu_1 + \mu_2) = 15$
glass beads	1	1	10^4	0	10^4

6.1. Results for constant toughness function: $k(\dot{z}, \alpha, t^*) = k_{\mathcal{S}}^0 = G_c$

We begin by presenting simulations for the basic case when the toughness function $k(\dot{z}, \alpha, t^*)$ is constant and identical for fracture and healing, namely, $k(\dot{z}, \alpha, t^*) = k_{\mathcal{S}}^0 = G_c$. As discussed in Remark 4, featuring the same constant value of toughness for fracture and healing implies that neither of these processes incurs any energy dissipation.

Figure 5 shows contour plots of the phase-field variable in the undeformed and the deformed configurations of a specimen, with bead diameter $D_0 = 2.3$ mm, gap-to-diameter ratio $H_0/D_0 = 0.21$, made of PDMS 45:1 with constant toughness $k(\dot{z}, \alpha, t^*) = k_{\mathcal{S}}^0 = G_c = 5$ J/m^2, and force parameter $\gamma = 3$, at three different values of the applied displacement $u = 5.33$, 5.35, and 5.46 mm. The corresponding values of the average stretch between the beads, namely, $\bar{\lambda} = 2.74$, 3.06, and 5.21, are also displayed in the plots in order to provide a more quantitative insight into the deformation field.

As illustrated by Fig. 5(a), following a large elastic deformation, two symmetric cracks are nucleated near the poles of the beads, where the hydrostatic stress happens to be about the largest in the specimen. Upon further loading, the two nucleated cracks propagate symmetrically in the transverse direction to the applied displacement, first slightly towards the midpoint between the beads and then away from it. Figures 5(b) and (c) show two snapshots of this propagation when the cracks are about 200 μm and 2 mm long, respectively. A number of simulations, not reported here, have shown that the above-outlined sequence of events are qualitatively insensitive to the value of the regularization parameter ε; quantitatively, however, smaller values of ε lead to larger applied displacements u at which fracture nucleates near the poles of the beads. On the other hand, the results are highly sensitive to the values of the constant toughness $k(\dot{z}, \alpha, t^*) = k_{\mathcal{S}}^0 = G_c$ of the PDMS and of the force parameter γ. This sensitivity is illustrated by the contour plots displayed in Figs. 6 and 7, which correspond to analogous simulations to those shown in Fig. 5 — that is, for bead diameter $D_0 = 2.3$ mm, gap-to-diameter ratio $H_0/D_0 = 0.21$, and PDMS 45:1 — but for two different sets of values of G_c and γ.

An immediate observation from Fig. 6 is that the results for the larger toughness $G_c = 10$ J/m^2 are essentially the same as those for $G_c = 5$ J/m^2 shown in Fig. 5, with the sole difference that the nucleation

---

[12]The attentive reader will have noted that we are making use of a trivial extension of the theory to the case of heterogeneous material properties.
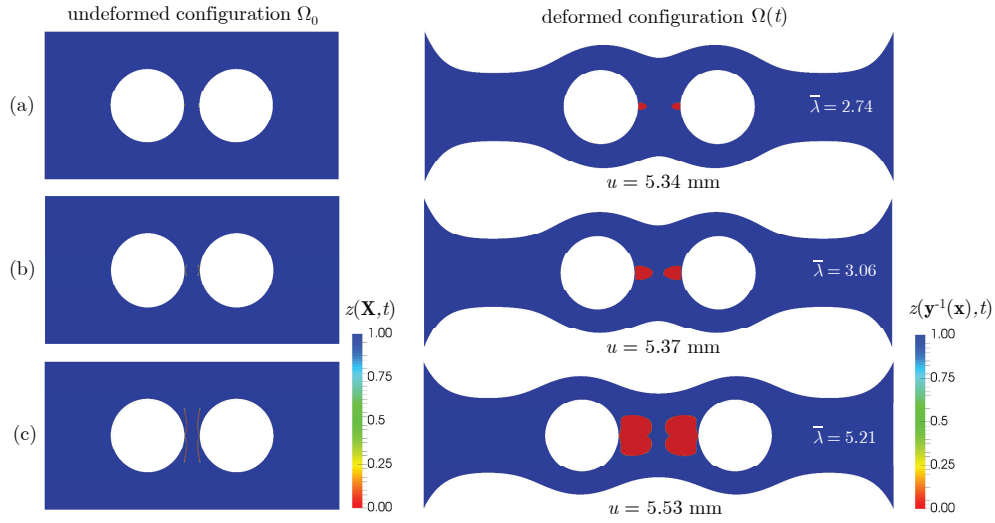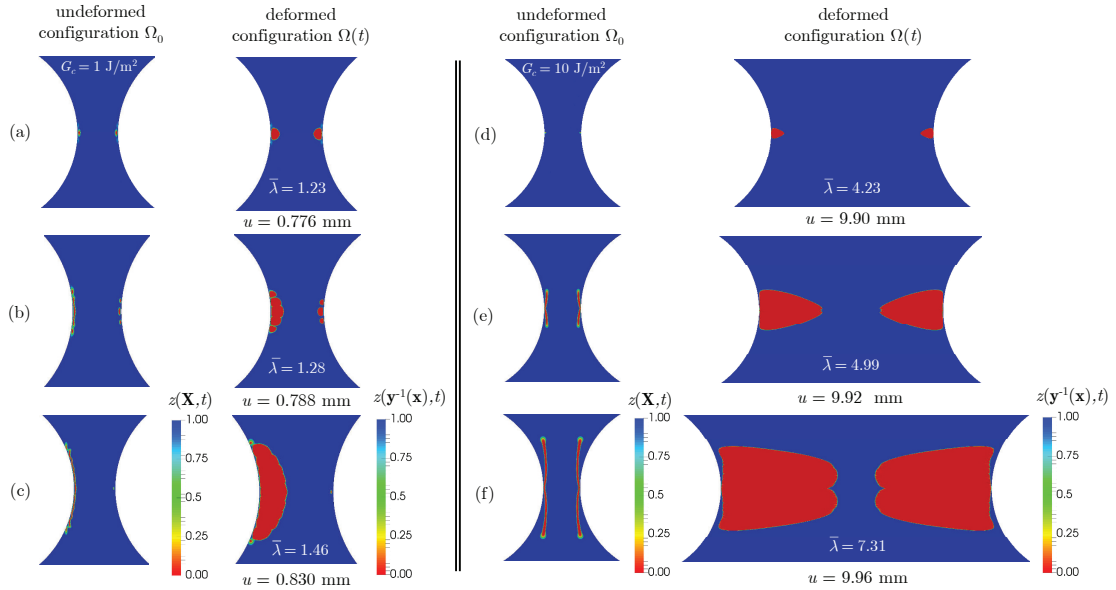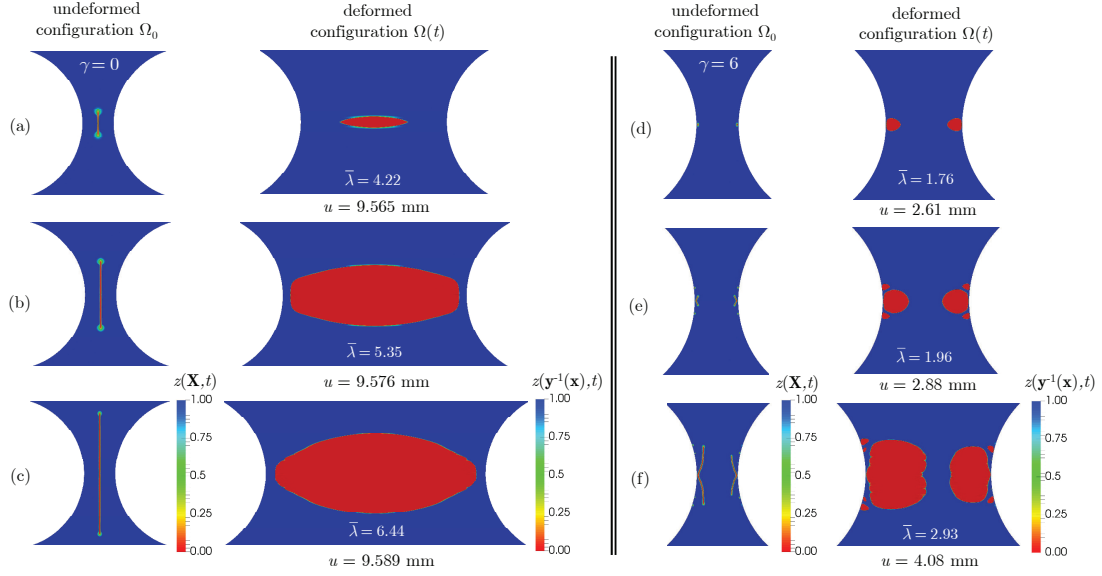
Figure 5: Simulation of the Gent-Park experiment for the case of bead diameter $D_0 = 2.3$ mm, gap-to-diameter ratio $H_0/D_0 = 0.21$, PDMS 45:1 with constant toughness $k(\dot{z}, \alpha, t^*) = k_{\mathcal{S}}^0 = G_c = 5$ J/m^2, and force parameter $\gamma = 3$. The plots correspond to contours of the phase field in the undeformed and the deformed configurations at three different values of the applied displacement u: (a) marginally after the nucleation of fracture has occurred ($u = 5.33$ mm), and (b)–(c) when the two nucleated cracks near the poles of the beads have propagated to reach sizes of roughly 200 μm ($u = 5.35$ mm) and the diameter of the beads ($u = 5.46$ mm). For completeness, the corresponding average stretch $\overline{\lambda}$ between the beads is also displayed in these and subsequent contour plots.

Figure 6: Simulations of the Gent-Park experiment for the cases of bead diameter $D_0 = 2.3$ mm, gap-to-diameter ratio $H_0/D_0 = 0.21$, force parameter $\gamma = 3$, and PDMS 45:1 with two different values of constant toughness: (a)–(c) $k(\dot{z}, \alpha, t^*) = k_{\mathcal{S}}^0 = G_c = 1$ J/m^2 and (d)–(f) $k(\dot{z}, \alpha, t^*) = k_{\mathcal{S}}^0 = G_c = 10$ J/m^2. The plots correspond to contours of the phase field in the undeformed and the deformed configurations of the PDMS region between the beads at three different values of the applied displacement u.

and propagation of the two cracks occur at larger applied displacements u. On the other hand, the results for the smaller toughness $G_c = 1$ J/m^2 are drastically different. Indeed, as illustrated by Fig. 6(a), two symmetric cracks are first nucleated near the poles of the beads at a smaller applied displacement u than that observed for $G_c = 5$ J/m^2 in Fig. 5. This is immediately followed by the nucleation of four more
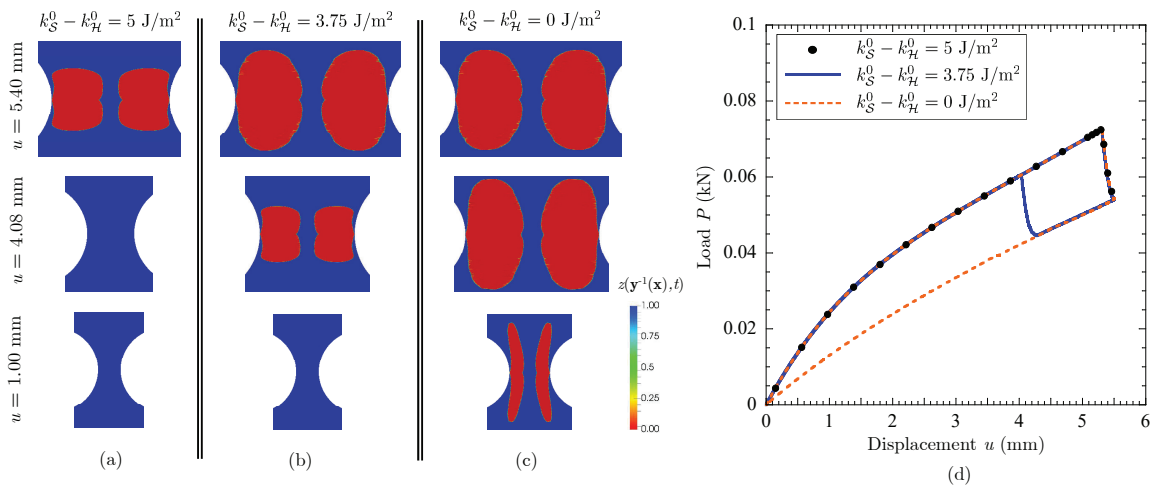
25

Figure 7: Simulations of the Gent-Park experiment for the cases of bead diameter $D_0 = 2.3$ mm, gap-to-diameter ratio $H_0/D_0 = 0.21$, PDMS 45:1 with constant toughness $k(\dot{z}, \alpha, t^*) = k_{\mathcal{S}}^0 = G_c = 5$ J/m^2, and two different values of the force parameter: (a)–(c) $\gamma = 0$ and (d)–(f) $\gamma = 6$. The plots correspond to contours of the phase field in the undeformed and the deformed configurations of the PDMS region between the beads at three different values of the applied displacement u.

symmetric cracks along the beads-PDMS interfaces. Upon further loading, the three nucleated cracks near the left bead coalesce and two more cracks are nucleated next to them along the bead-PDMS interface, while the three nucleated cracks near the right bead start healing. This is illustrated by Fig. 6(b). This trend of coalescence and nucleation of more cracks along the left bead-PDMS interface together with healing of the cracks near the right bead continues upon further loading. This is illustrated by the contour plots in Fig. 6(c), which correspond to the applied displacement $u = 0.771$ mm at which the cracks near the right bead have just about completely healed. The reason why the cracks near the left bead coalesce and nucleate while those near the right bead heal, and not viceversa, is purely stochastic in nature. Indeed, when the same simulation is carried out on a different random finite-element discretization, the same solution is obtained up to a reflection around the symmetry axis transverse to the direction of the applied displacement.

Figure 7 shows that the results for smaller and larger values of the force parameter, $\gamma = 0$ and $\gamma = 6$, are also drastically different from those for $\gamma = 3$ shown in Fig. 5. Specifically, for the smaller parameter $\gamma = 0$, it is seen from Fig. 7(a) that a single crack nucleates at the midpoint between the beads at a larger applied displacement u than that obtained for $\gamma = 3$ in Fig. 5. This drastic difference in where and when fracture first nucleates can be understood at once by recognizing that the strain energy is largest at the midpoint between the beads and, since in this case (because $\gamma = 0$) the hydrostatic stress does not contribute to the nucleation of fracture (see Remark 5), it is there that the nucleation of a crack occurs first. Figures 7(b) and (c) show that the single nucleated crack propagates by increasing the applied displacement in the direction transverse to it. For the larger force parameter $\gamma = 6$, by contrast, it is seen from Fig. 7(d) that two cracks are first nucleated near the poles of the beads, much like in the case of $\gamma = 3$ shown in Fig. 5 but at a smaller applied displacement u. Further loading leads to the propagation of the two cracks in the transverse direction to the applied displacement together with the nucleation of four more symmetric cracks along the beads-PDMS interfaces. A snapshot of this is shown by Fig. 7(e). Upon further loading, the two cracks near the poles continue to propagate in the transverse direction to the applied displacement, the secondary cracks start healing, and more symmetric cracks continue to nucleate along the beads-PDMS interfaces. While this trend is initially symmetric, at a sufficiently large applied load the cracks near one of the beads propagate and nucleate at a lower rate and eventually all of them start healing. This is illustrated by the contour plots in Fig. 7(f), which correspond to the applied displacement $u = 4.08$ mm at which the cracks near the right

26

bead start exhibiting a lower rate of propagation and nucleation. This too is a stochastic process, as the same simulation leads to the same solution up to a reflection around the symmetry axis transverse to the direction of the applied displacement when carried out on different random finite-element discretizations.

6.2. Results for piecewise constant toughness function

We now turn to the case when the toughness function $k(\dot{z}, \alpha, t^*)$ takes on different constant values for fracture and for healing. Recall from Remark 4 that, for such a case, we have $k(\dot{z}, \alpha, t^*) = k_{\mathcal{S}}^0 + k_{\mathcal{F}}^0 = G_c \geq 0$ at the points where z decreases, while $k(\dot{z}, \alpha, t^*) = k_{\mathcal{S}}^0 - k_{\mathcal{H}}^0 \leq G_c$ at those where z increases. Furthermore, fracture and healing both participate in energy dissipation, provided that $k_{\mathcal{F}}^0, k_{\mathcal{H}}^0 > 0$, and non-positive values of the toughness function for the healing branch imply that healing is prohibited, or in other words, that fracture is irreversible.

Figure 8: Simulations of the Gent-Park experiment for the cases of bead diameter $D_0 = 2.3$ mm, gap-to-diameter ratio $H_0/D_0 = 0.21$, force parameter $\gamma = 3$, and PDMS 45:1 with constant fracture toughness $k_{\mathcal{S}}^0 + k_{\mathcal{F}}^0 = G_c = 5$ J/m^2 and three different constant values of healing toughness $k_{\mathcal{S}}^0 - k_{\mathcal{H}}^0 = 5, 3.75,$ and 0 J/m^2. (a)–(c) Contour plots of the phase field in the deformed configuration of the PDMS region between the beads at three different values of the applied displacement u during the unloading of the three specimens. (d) Plots of the computed load P as a function of the applied displacement u for the entire process of the loading and unloading of the three specimens.

Figure 8 presents results from simulations of the loading up to a maximum applied displacement of $u = 5.50$ mm and subsequent complete unloading to $u = 0$ mm of three specimens with bead diameter $D_0 = 2.3$ mm, gap-to-diameter ratio $H_0/D_0 = 0.21$, force parameter $\gamma = 3$, and PDMS 45:1 featuring three different piecewise constant toughness functions $k(\dot{z}, \alpha, t^*)$. Specifically, all three specimens feature the same constant toughness $k(\dot{z}, \alpha, t^*) = k_{\mathcal{S}}^0 + k_{\mathcal{F}}^0 = G_c = 5$ J/m^2 when $\dot{z} \leq 0$, but the different constant toughness $k(\dot{z}, \alpha, t^*) = k_{\mathcal{S}}^0 - k_{\mathcal{H}}^0 = 5, 3.75,$ and 0 J/m^2 for the healing branch when $\dot{z} > 0$. Parts (a)–(c) of the figure display contour plots of the phase-field variable in the deformed configuration of the PDMS region between the beads at the applied displacements $u = 5.40, 4.08, 1.00$ mm during the unloading, while part (d) presents the comparison of the complete load-displacement (P vs. u) responses for all three specimens.

As expected on physical grounds, the results in Fig. 8 show that the responses of all three specimens are indistinguishable from one another during the entire loading process up to the maximum applied displacement $u = 5.50$ mm. The responses during the unloading are, also as expected, different. Specifically, we note from Fig. 8(d) that the load-displacement response of the specimen with $k_{\mathcal{S}}^0 - k_{\mathcal{H}}^0 = 5$ J/m^2 exhibits no hysteresis. This is consistent with the fact that the two cracks nucleated near the poles in that specimen completely heal by following exactly the same path as in their fracturing. By contrast, the specimens with $k_{\mathcal{S}}^0 - k_{\mathcal{H}}^0 = 3.75$ and 0 J/m^2 do exhibit significant hystereses. In particular, upon unloading, the two cracks nucleated near the poles in the specimen with $k_{\mathcal{S}}^0 - k_{\mathcal{H}}^0 = 3.75$ J/m^2 do not heal but simply deform elastically

27

up to a displacement of about $u = 4.25$ mm, at which point they start to heal. At a displacement of about $u = 4.00$ mm, the two cracks have completely healed. Upon further unloading, therefore, the specimen simply deforms elastically. On the other hand, the two cracks nucleated near the poles in the specimen with $k_{\mathcal{S}}^0 - k_{\mathcal{H}}^0 = 0$ J/m^2 never heal, but simply deform upon unloading.

6.3. Results for evolving toughness function

We finally turn to two sample simulations that showcase the response of specimens wherein the toughness function $k(\dot{z}, \alpha, t^*)$ evolves in regions that experience healing.

Figure 9 presents results from the simulation of the loading up to a maximum applied displacement of $u = 5.50$ mm, subsequent complete unloading to $u = 0$ mm, reloading up to a maximum applied displacement of $u = 5.34$ mm, and subsequent unloading to $u = 0$ mm of a specimen with bead diameter $D_0 = 2.3$ mm, gap-to-diameter ratio $H_0/D_0 = 0.21$, force parameter $\gamma = 3$, and PDMS 45:1 featuring the following toughness function:

$$k(\dot{z}, \alpha, t^*) = \begin{cases} [5 - 0.125\,\alpha(\mathbf{X}, t^*(\mathbf{X}, t))] \text{ J/m}^2 & \text{if} \quad \dot{z} \leq 0 \\[2mm] [3.75 - 0.094\,\alpha(\mathbf{X}, t^*(\mathbf{X}, t))] \text{ J/m}^2 & \text{if} \quad \dot{z} > 0 \end{cases}. \tag{45}$$

Note that the value of the toughness function (45) evolves with the cumulative history of fracture and healing in both of its branches. In particular, the value of the fracture toughness decreases by 5% of its initial value of 5 J/m^2, while that of the healing toughness decreases by the same percentage of its initial value of 3.75 J/m^2 at every material point $\mathbf{X}$ that experiences a complete cycle of fracturing and healing.

The chief observation from Fig. 9 is that, due to the decrease in fracture toughness from 5 J/m^2 to 4.75 J/m^2 in the regions of the elastomer that fractured and healed in the first cycle of loading and unloading, the nucleation and propagation of fracture in the second cycle of loading occur at the same locations as in the first cycle, but at smaller applied displacements u. By the same token, due to the decrease in healing toughness from 3.75 J/m^2 to 3.56 J/m^2 in the regions of the elastomer that fractured and healed in the first cycle of loading and unloading, the healing in the second cycle of unloading occurs at smaller applied displacements u than in the first cycle.

Analogous to the results displayed in Fig. 9, Fig. 10 presents results from the simulation of the loading up to a maximum applied displacement of $u = 5.50$ mm, subsequent complete unloading to $u = 0$ mm,
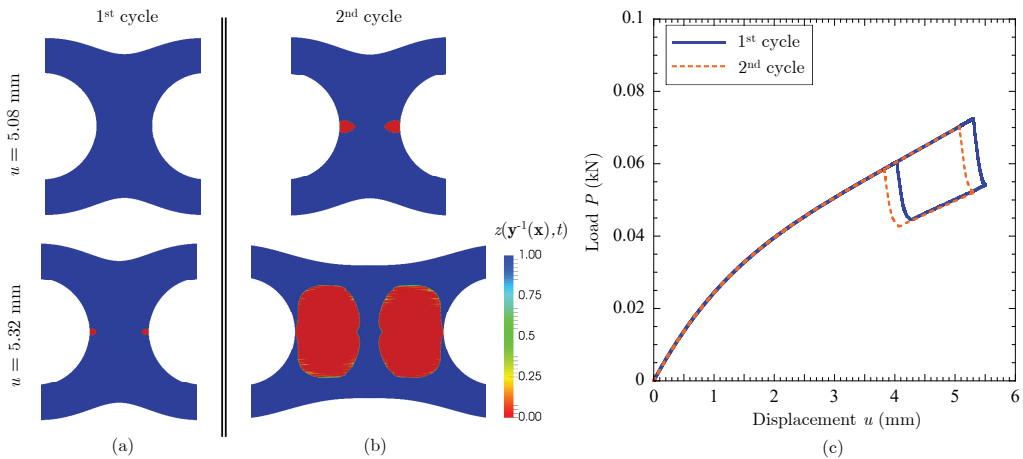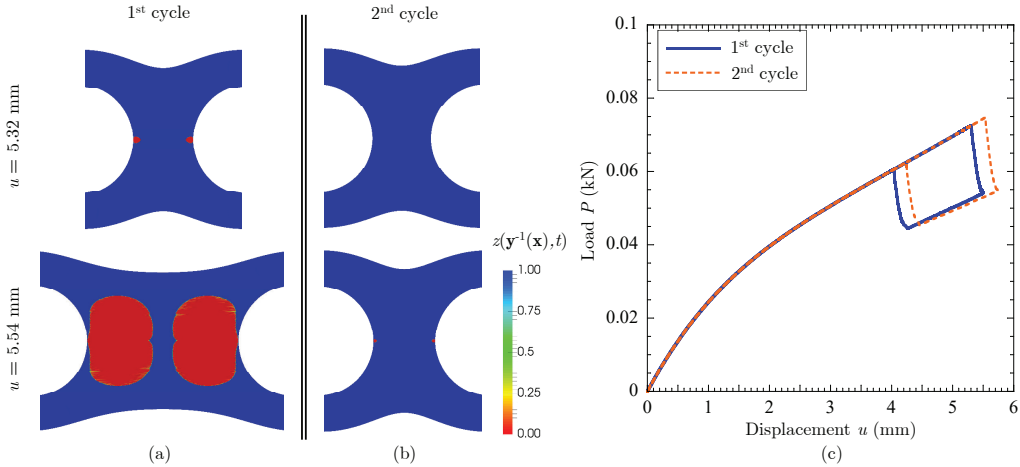

Figure 9: Simulations of the Gent-Park experiment for two successive cycles of loading and unloading of a specimen with bead diameter $D_0 = 2.3$ mm, gap-to-diameter ratio $H_0/D_0 = 0.21$, force parameter $\gamma = 3$, and PDMS 45:1 with the decreasing toughness function (45). (a)–(b) Contour plots of the phase field in the deformed configuration of the PDMS region between the beads at two different values of the applied displacement u during the first and the second loading. (c) Plots of the computed load P as a function of the applied displacement u for the two cycles of loading and unloading of the specimen.

28

Figure 10: Simulations of the Gent-Park experiment for two successive cycles of loading and unloading of a specimen with bead diameter $D_0 = 2.3$ mm, gap-to-diameter ratio $H_0/D_0 = 0.21$, force parameter $\gamma = 3$, and PDMS 45:1 with the increasing toughness function (46). (a)–(b) Contour plots of the phase field in the deformed configuration of the PDMS region between the beads at two different values of the applied displacement u during the first and the second loading. (c) Plots of the computed load P as a function of the applied displacement u for the two cycles of loading and unloading of the specimen.

reloading up to a maximum applied displacement of $u = 5.74$ mm, and subsequent unloading to $u = 0$ mm of a specimen with the same bead diameter D_0, gap-to-diameter ratio H_0/D_0, and force parameter γ as that in Fig. 9, but with a PDMS 45:1 elastomer that features the different toughness function

$$
k(\dot{z}, \alpha, t^*) = \begin{cases} [5 + 0.125\,\alpha(\mathbf{X}, t^*(\mathbf{X}, t))] \ \text{J/m}^2 & \text{if} \quad \dot{z} \leq 0 \\[2mm] [3.75 + 0.094\,\alpha(\mathbf{X}, t^*(\mathbf{X}, t))] \ \text{J/m}^2 & \text{if} \quad \dot{z} > 0 \end{cases}.
\tag{46}
$$

In particular, the values of both branches in the toughness function (46), contrary to those is (45), increase with the cumulative history of fracture and healing: while the fracture toughness increases by 5% of its initial value of 5 J/m^2, the healing toughness increases by the same percentage of its initial value of 3.75 J/m^2 at every material point $\mathbf{X}$ that experiences a complete cycle of fracturing and healing.

Consistent with the fact that the fracture toughness and the healing toughness increase from 5 J/m^2 to 4.75 J/m^2 and from 3.75 J/m^2 to 3.94 J/m^2 in the regions of the elastomer that fractured and healed in the first cycle of loading and unloading, Fig. 10 shows that the nucleation and propagation of fracture and healing in the second cycle of loading and unloading occur at the same locations as in the first cycle, but at larger applied displacements u.

7. Comparisons with the experiments of Poulain et al. (2017) and final comments

The above sample results have provided evidence that the proposed theory (and associated numerical implementation) has the capability to describe all the various complex features of the nucleation and propagation of fracture and healing in elastomers that were noted in the Introduction, at least qualitatively. In this section, through direct comparisons with the recent Gent-Park experiments of Poulain et al. (2017), we provide a more quantitative set of evidence to further support the relevance of the theory to describe, explain, and predict the phenomena of fracture and healing in elastomers.

We begin by comparing in Fig. 11 contour plots (in the deformed configuration) of the phase-field variable predicted by the theory with corresponding snapshots from the Gent-Park experiment presented in Figs. 5 and 6 in Section 5 of Poulain et al. (2017). The specimen there is made of a PDMS elastomer with a 15:1 ratio of base to curing agent, the glass beads have a diameter of $D_0 = 3.178$ mm and are set apart by an
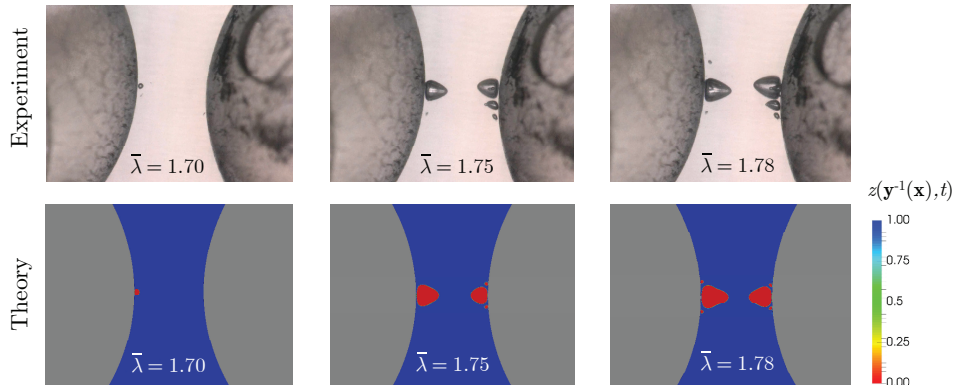
Figure 11: Comparison of the proposed theory with a Gent-Park experiment in Poulain et al. (2017) for a specimen, with bead diameter $D_0 = 3.178$ mm and gap between the beads $H_0 = 0.340$, made of a PDMS elastomer with a 15:1 ratio of base to curing agent.

initial gap of $H_0 = 0.340$ mm. In the simulation, accordingly, we have taken the nonlinear elastic response of the elastomer to be characterized by the stored-energy functions (44) with material parameters $\beta_1 = 0.2274$, $\beta_2 = 4.5394$, $\mu_1 = 0.2696$ MPa, $\mu_2 = 0.0441$ MPa, and compressibility parameter $\kappa = 10^3(\mu_1 + \mu_2) = 313.7$ MPa. This choice describes accurately the uniaxial stress-stretch response at quasistatic stretch rates of the grade of PDMS 15:1 utilized in the experiment. We have also taken the fracture and healing properties to be characterized by the constant toughness function $k(\dot{z}, \alpha, t^*) = k_{\mathcal{S}}^0 = G_c = 60$ J/m^2. Given that there is no direct experimental knowledge of the fracture and healing properties of PDMS 15:1, this specific choice of toughness function is used because, in addition to being plausible, leads to results that agree with the experimental observations. Furthermore, the force parameter γ used in the simulation is taken not to have a constant value throughout the entire specimen, but, instead, to have spatially random heterogeneous values in the range $[3.0, 3.6]$. This is because, as elaborated in the Appendix, the value of the parameter γ is expected to depend on the size of the microscopic defects from which fracture initiates, and these are known to exhibit a stochastic spatial variation in actual elastomers (see, e.g., Gent, 1990). Finally, we note that the simulation was carried with $\mathbf{b}(\mathbf{X}, t) = \mathbf{0}$, $\varepsilon = 5$ μm, $\eta_W = 10^{-3}$, $\eta_\kappa = 10^{-6}$, $\nu = 10^2 \max\{k(\dot{z}, \alpha, t^*)\}/\varepsilon$, in an uniform axisymmetric mesh of size $h = \varepsilon/3 = 1.67$ μm in the PDMS region between the beads.

The immediate observation from Fig. 11 is that the theory is able to describe fairly accurately the first nucleation of fracture near the pole of the left bead, as well as its growth, deformation, and subsequent nucleation of multiple cracks near both of the beads upon further loading. We emphasize that the fact that the theory is able to predict the first nucleation of fracture near the pole of the left bead, as opposed to near the pole of the right bead, is because the value of the force parameter γ is slightly larger there. The same argument explains the secondary nucleation of multiple cracks near the right bead, as opposed to near the left bead. As discussed in the Appendix, this would imply that the underlying microscopic defects from which fracture initiates in the actual elastomer are slightly larger than their counterparts near the opposite bead.

We now turn to the analogous comparison shown in Fig. 12 between the theory and the Gent-Park experiment presented in Fig. 9 in Section 5 of Poulain et al. (2017). In that case, the specimen is made of a different PDMS elastomer featuring a 45:1 ratio of base to curing agent, the glass beads are of a smaller diameter and the gap between them is larger, specifically, $D_0 = 2.286$ mm and $H_0 = 0.480$ mm. In the simulation of this experiment, the nonlinear elastic response of the elastomer is characterized by the stored-energy functions (44) with the material parameters indicated in Table 1, the fracture and healing properties are characterized by the constant toughness function $k(\dot{z}, \alpha, t^*) = k_{\mathcal{S}}^0 = G_c = 5$ J/m^2, and the force parameter γ varies randomly in space taking values in the range $[2.8, 2.9]$. All the other parameters used in the simulation are identical to those used in the preceding comparison.

Similar to the results presented in Fig. 11, the results in Fig. 12 show that the theory describes fairly
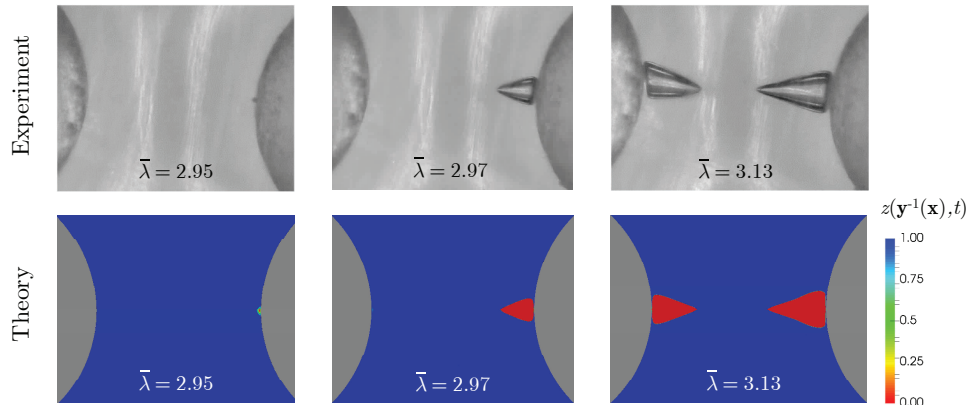
Figure 12: Comparison of the proposed theory with a Gent-Park experiment in Poulain et al. (2017) for a specimen, with bead diameter $D_0 = 2.286$ mm and gap between the beads $H_0 = 0.480$, made of a PDMS elastomer with a 45:1 ratio of base to curing agent.

accurately the experimental observations, from the first nucleation of a crack near the pole of the right bead, to its growth and conical deformation upon further loading, to the later nucleation and growth of a second crack near the pole of the left bead upon yet further loading. Again, the fact that the theory predicts the first nucleation of a crack near the pole of the right bead, as opposed to near the pole of the left bead, is because the value of the force parameter γ is slightly larger there. This would imply that the underlying microscopic defect from which fracture initiates in the actual elastomer is slightly larger than its counterpart near the left bead.

The above comparisons with experiments, together with the preceding sample simulations, point to the potential of the proposed theory. They also make it plain that experiments that probe independently the nucleation of cracks, their propagation, and their healing are of the essence to understand the fracture and healing properties of a given elastomer of interest. Such experiments along with more thorough comparisons with the proposed theory will be the subject of future work.

Acknowledgements

Appendix. On the microscopic origins of the macroscopic external force c_{e}

In this appendix, we present results that shed light on the microscopic origins of the external force (18), posited on purely macroscopic grounds in the main body of the text.

Following the guiding principle that the nucleation of macroscopic fracture stems from the fracture that initiates from inherent microscopic defects, we consider the fundamental boundary-value problem schematically depicted in Fig. 13 — namely, the isotropic stretch of a small spherical ball made out of a homogeneous elastomer — from macroscopic and microscopic points of view. The problem depicted in Fig. 13(a) represents the macroscopic view adopted in this paper, wherein the presence of microscopic defects in elastomers is accounted for implicitly by the incorporation of the external force (18) in the governing equation (21) for the phase-field variable $z(\mathbf{X}, t)$. On the other hand, the problem depicted in Fig. 13(b) represents the microscopic view of the same problem, wherein the presence of defects is accounted for explicitly and, consequently, no incorporation of an external force is required. In the sequel, we demonstrate via sample results that the initiation of fracture from the microscopic defect in the boundary-value problem depicted in

31

Fig. 13(b) can indeed be described as the nucleation of macroscopic fracture in the boundary-value problem depicted in Fig. 13(a), so long as the external force (18) is taken into account in the latter.

Before proceeding with the results *per se*, we remark that the critical stretch, λ_{cr} say, at which fracture nucleates in the ball without the defect can be determined analytically. Indeed, assuming that the nucleation of fracture occurs uniformly throughout, it is straightforward to deduce from the governing equations (20)–(21) that fracture first nucleates in the defect-free ball at the critical stretch λ_{cr} given by the smallest positive root of the nonlinear algebraic equation

$$\mathcal{C}(\lambda_{cr}) \doteq \frac{8}{3}\left(W(\lambda_{cr}\mathbf{I}) + \kappa g(\lambda_{cr}\mathbf{I})\right) + \frac{4\gamma}{9\lambda_{cr}^p}\left(\frac{\kappa}{\lambda_{cr}^2}\mathbf{I}\cdot\frac{\partial g}{\partial\mathbf{F}}(\lambda_{cr}\mathbf{I})\right) - \frac{k_\mathcal{S}^0 + k_\mathcal{F}^0}{2\varepsilon} = 0. \tag{47}$$

For later use, assuming that the body force $\mathbf{b}(\mathbf{X},t) = \mathbf{0}$, we note that the corresponding critical Cauchy hydrostatic pressure on the boundary of the ball at which fracture first nucleates is given by

$$\mathcal{P}_{cr} = \frac{1}{3\lambda_{cr}^2}\text{tr}\left(\frac{\partial W}{\partial\mathbf{F}}(\lambda_{cr}\mathbf{I}) + \kappa\frac{\partial g}{\partial\mathbf{F}}(\lambda_{cr}\mathbf{I})\right), \tag{48}$$

where λ_{cr} stands for the critical stretch implicitly defined by (47). By contrast, the critical stretch λ_{cr} and, by the same token, the corresponding critical Cauchy hydrostatic pressure $\mathcal{P}_{cr}$ at which fracture initiates in the ball containing the defect must be determined through the numerical solution of the corresponding governing equations (20)–(21), that is, with the contribution from the external force $c_\mathbf{e}$ removed.

Figure 14 shows sample comparisons between the critical pressures $\mathcal{P}_{cr}$ at which fracture nucleates in the defect-free ball (solid lines) and at which fracture initiates in the ball containing the defect (solid circles). The results pertain to a ball of radius $R_0 = 0.5$ mm and the same type of PDMS 45:1 elastomer considered in Section 6, with stored-energy functions (44) and the material parameters β_1, β_2, μ_1, μ_2 listed in Table 1, featuring constant toughness function $k(\dot{z},\alpha,t^*) = k_\mathcal{S}^0 = G_c = 1$ J/m^2 and compressibility parameters ranging from $\kappa = \mu_1 + \mu_2 = 0.015$ MPa to $\kappa = 10^3(\mu_1 + \mu_2) = 15$ MPa; recall that the combination $\mu_1 + \mu_2$ stands for the initial shear modulus of the elastomer. More specifically, the simulations for the ball with the defect correspond to a defect diameter of $\delta = 1$ μm, parameters $\varepsilon = \delta/20 = 0.05$ μm, $\eta_W = 10^{-3}$, $\eta_\kappa = 10^{-6}$, $\nu = 10^2\max\{k(\dot{z},\alpha,t^*)\}/\varepsilon$, and a uniform fine mesh of size $h = \varepsilon/3 = 0.017$ μm near the defect. On the other hand, the results for the ball without the defect corres pond to two choices of the external force, $c_\mathbf{e} = 0$ and $c_\mathbf{e} \neq 0$ given by expression (18) with the parameter γ depicted in Fig. 15, and $\varepsilon = 5$ μm. This specific value of ε was selected so as to be of the same order of magnitude as the size of the defect δ and also, for definiteness, to make the critical pressures for fracture nucleation in the macroscopic problem and fracture initiation from the defect in the microscopic problem match (at $\mathcal{P}_{cr} = 2.39(\mu_1 + \mu_2)$) for the case of $\kappa/(\mu_1 + \mu_2) = 1$.
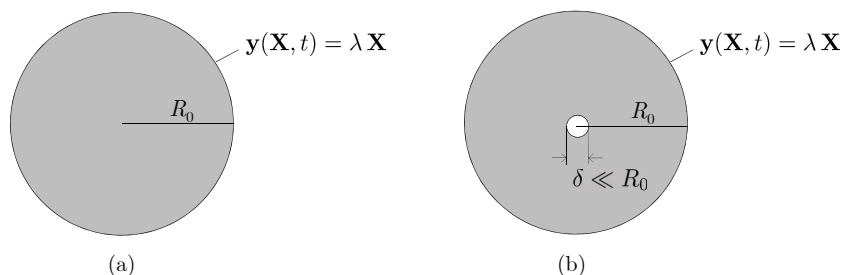

Figure 13: Schematics of the undeformed geometries of (a) a defect-free spherical ball of initial radius R_0 and (b) a spherical ball of the same initial radius R_0 that contains a vacuous spherical defect of diameter $\delta \ll R_0$ at its center. Both specimens are made out of the same homogenous elastomer and are subjected to the same isotropic stretch λ on their boundaries. While the boundary-value problem depicted in (a) represents the macroscopic view adopted in the present work, wherein microscopic defects are accounted for implicitly by the incorporation of an external force $c_\mathbf{e}$, the equivalent boundary-value problem depicted in (b) represents its corresponding microscopic view, wherein defects are accounted for explicitly and the external force $c_\mathbf{e}$ is therefore absent.
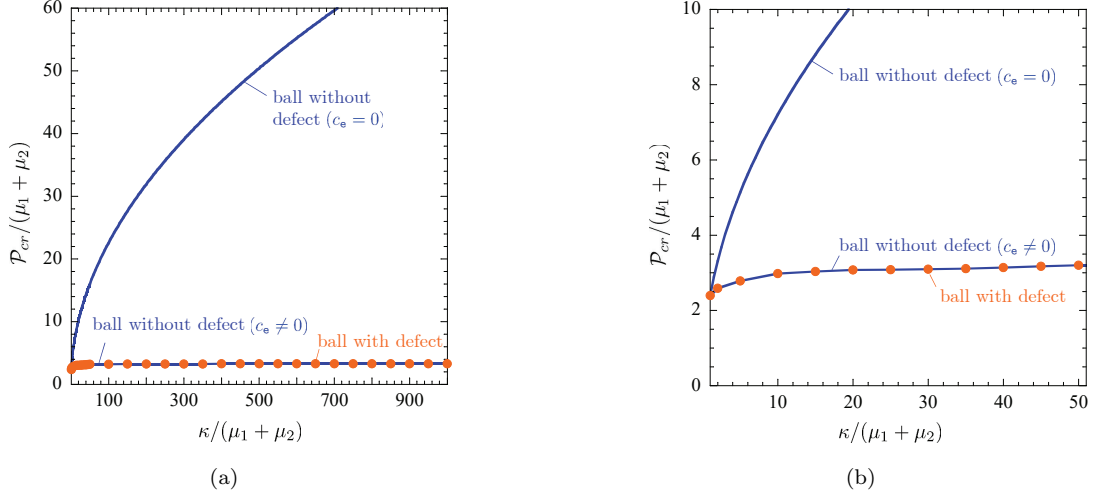
Figure 14: Comparison between the critical pressures $\mathcal{P}_{cr}$ at which fracture nucleates in the defect-free ball (solid lines) and at which fracture initiates in the ball that contains the defect (solid circles). The plots show $\mathcal{P}_{cr}$, normalized by the initial shear modulus $\mu_1 + \mu_2$ of the elastomer, as a function of the compressibility parameter κ of the elastomer, also normalized by its initial shear modulus. Part (a) presents results from the high-compressibility value of $\kappa/(\mu_1 + \mu_2) = 1$ to the near-incompressibility value of $\kappa/(\mu_1 + \mu_2) = 10^3$, while part (b) displays a zoom-in of the results in the range $\kappa/(\mu_1 + \mu_2) \in [1, 50]$.
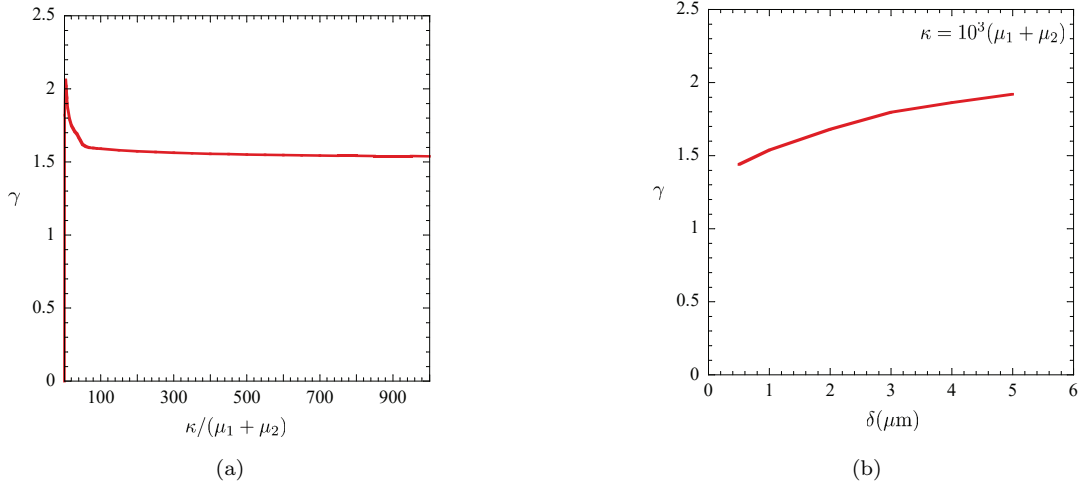

Figure 15: (a) The parameter γ in the external force (18) utilized to match the result for the nucleation of macroscopic fracture in the defect-free ball with the result for the initiation of microscopic fracture in the ball with the defect in Fig. 14. (b) The parameter γ required in the external force (18) to match the critical pressures $\mathcal{P}_{cr}$ at which fracture nucleates in the defect-free ball and at which fracture initiates in balls that contain a the defect of diameter δ for the case of a PDMS 45:1 elastomer with compressibility parameter $\kappa = 10^3(\mu_1 + \mu_2)$.

Save for the case of elastomers featuring unrealistically high compressibility, it is apparent from Fig. 14 that the initiation of fracture in the ball containing the defect cannot possibly be described as the nucleation of fracture in the defect-free ball without taking into account the presence of an external force $c_{\mathbf{e}}$. Moreover, Fig. 14 illustrates that the form (18) proposed for $c_{\mathbf{e}}$ in this work can lead to a nucleation of macroscopic fracture that fully agrees with the initiation of fracture from microscopic defects by appropriately selecting the value of the parameter γ.

Now, as indicated in the main body of the text, the appropriate selection of the value of the parameter

γ for a given elastomer is strongly dependent on the compressibility of the elastomer. This point is clearly illustrated by Fig. 15(a), where γ is seen to be vanishingly small when the elastomer is highly compressible $(\kappa/(\mu_1+\mu_2) \approx 1)$ and of order one when the elastomer exhibits moderate compressibility $(\kappa/(\mu_1+\mu_2) \approx 10)$ or near incompressibility $(\kappa/(\mu_1+\mu_2) > 100)$. The selection of the parameter γ is also dependent on the size of the microscopic defects from which fracture initiates in the given elastomer. This point is illustrated by Fig. 15(b), which presents the values of γ required in the external force (18) to match the nucleation of fracture in the same defect-free ball considered in Fig.14 with the initiation of fracture in balls that contain a defect of diameters ranging from $\delta = 0.5$ μm to 5.0 μm for the case of a nearly incompressible PDMS 45:1 elastomer with compressibility parameter $\kappa = 10^3(\mu_1+\mu_2)$. A number of simulations, not reported here, have shown that γ depends as well on the shape of the defects from which fracture initiates, but that such a dependence is much weaker than the one on their size. We close by remarking that the above-outlined dependence of γ on the geometry of the microscopic defects from which fracture initiates suggests that this parameter is stochastic in nature, as defects in specimens made out of actual elastomers are known to exhibit a range of sizes and, to a lesser extent, shapes (Gent, 1990).

References

Andrews, E.H., 1963. Rupture propagation in hysteresial materials: Stress at a notch. *Journal of the Mechanics and Physics of Solids* 11, 231–242.

Babuska, I., Zlamal, M., 1973. Nonconforming elements in the finite element method with penalty. *SIAM J. Numer. Anal.* 10, 863–875.

Bahrt Madsen, F., Yu, L., Ladegaard Skov, A., 2016. Self-healing, high-permittivity silicone dielectric elastomer. *ACS Macro Letters* 5, 1196–1200.

Ball, J.M., 1982. Discontinuous equilibrium solutions and cavitation in nonlinear elasticity. *Philos. Trans. R. Soc. Lond.* 306, 557–610.

Behrman, W., 1998. *An Efficient Gradient Flow Method for Unconstrained Optimization* (Ph.D. thesis). Stanford University.

Bischoff, J.E., Arruda, E.M., Grosh, K., 2001. A new constitutive model for the compressibility of elastomers at finite deformations. *Rubber Chem. Technol.* 74, 541–559.

Blaiszik, B.J., Kramer, S.L.B., Olugebefola, S.C., Moore, J.S., Sottos, N.R., White, S.R., 2010. Self-healing polymers and composites. *Annual Review of Materials Research* 40, 179–211.

Boffi, D., Brezzi, F., Fortin, M., 2013. *Mixed Finite Element Methods and Applications*. Springer, New York.

Bourdin, B., Francfort, G.A., Marigo, J.J., 2000. Numerical experiments in revisited brittle fracture. *Journal of the Mechanics and Physics of Solids* 48, 797–826.

Bourdin, B., Francfort, G.A., Marigo, J.J., 2008. The variational approach to fracture. *Journal of Elasticity* 91, 5–148.

Braides, A., 1998. *Approximation of Free-Discontinuity Problems*. Springer-Berlag, Berlin.

Braides, A., Dal Maso, G., Garroni, A.,1999. Variational formulation of softening phenomena in fracture mechanics: The one-dimensional case. *Archive for Rational Mechanics and Analysis* 146, 23–58.

Bridgman, P.W., 1945. The compression of sixty-one solid substances to 25,000 kg/cm, determined by a new rapid method. *Proc. Am. Acad. Arts Sci.* 76, 9–24.

Burman, E., Hansbo, P., 2005. Stabilized Crouzeix-Raviart element for the Darcy-Stokes problem. *Numerical Methods for Partial Differential Equations* 21, 986–997.

Cauchy, A., 1847. Méthode générale pour la résolution des systèmes d'équations simultanées. *Comptes Rendus Hebd. Séeances Acad. Sci.* 25, 536–538.

Cordier, P., Tournilhac, F., Soulie-Ziakovic C., Leibler, L., 2008. Self-healing and thermoreversible rubber from supramolecular assembly. *Nature* 451, 977–980.

Crouzeix, M., Raviart, P.-A., 1973. Conforming and nonconforming finite element methods for solving the stationary Stokes equations I. *Rev. Française Automat. Informat. Recherche Opérationnelle* 7, 33–75.

Del Piero, G., Lancioni, G., March, R., 2007. A variational model for fracture mechanics: Numerical experiments. *J. Mech. Phys. Solids* 55, 2513–2537.

Ericksen, J.L., 1975. Equilibrium of bars. *Journal of Elasticity* 5, 191–201.

Falk, R.S., 1991. Nonconforming finite element methods for the equations of linear elasticity. *Mathematics of Computation* 57, 529–55.

Farrell, P.E., Maurini, C., 2017. Linear and nonlinear solvers for variational phase-field models of brittle fracture. *International Journal for Numerical Methods in Engineering* 109, 648–667.

Fond, C., Lobbrecht, A., Schirrer, R., 1996. Polymers toughened with rubber microspheres: an analytical solution for stresses and strains in the rubber particles at equilibrium and rupture. *International Journalof Fracture* 77, 141–159.

Francfort, G.A., Marigo, J.J., 1998. Revisiting brittle fracture as an energy minimization problem. *Journal of the Mechanics and Physics of Solids* 46, 1319–1342.

Gao, H., Klein, P., 1998. Numerical simulation of crack growth in an isotropic solid with randomized internal cohesive bonds. *Journal of the Mechanics and Physics of Solids* 46, 187–218.

Gent, A.N., 1990. Cavitation in rubber: A cautionary tale. *Rubber Chemistry and Technology* 63, 49–53.

Gent, A.N., Lindley, P.B., 1959. Internal rupture of bonded rubber cylinders in tension. *Proc. R. Soc. A* 249, 195–205.

Gent, A.N., Park, B., 1984. Failure processes in elastomers at or near a rigid inclusion. *J. Mater. Sci.* 19, 1947–1956.

Gent, A.N., Wang, C., 1991. Fracture mechanics and cavitation in rubber-like solids. *Journal of Materials Science* 26, 3392–3395.

Gerasimov, T., De Lorenzis, L., 2016. A line search assisted monolithic approach for phase-field computing of brittle fracture. *Computer Methods in Applied Mechanics and Engineering* 312, 276–303.

Giacomini, A., 2005. Ambrosio-Tortorelli approximation of quasi-static evolution of brittle fractures. *Calc. Var. Partial Dif.* 22, 129–172.

Griffith, A.A., 1921. The phenomena of rupture and flow in solids. *Philos. Trans. R. Soc. Lond. A* 221, 163–198.

Gurtin, M.E., 1996. Generalized Ginzburg–Landau and Cahn–Hilliard equations based on a microforce balance. *Physica D* 92, 178–192.

Gurtin, M.E., 2000. *Configurational Forces as Basic Concepts of Continuum Physics*. Springer, New York.

Hackl, K., Fischer, F.D., 2008. On the relation between the principle of maximum dissipation and inelastic evolution given by dissipation potentials. *Proc. R. Soc. A* 464, 117–132.

Hackl, K., Fischer, F.D., Svoboda, J., 2011. A study on the principle of maximum dissipation for coupled and non-coupled non-isothermal processes in materials. *Proc. R. Soc. A* 467, 1186–1196.

Hansbo, P., Larson, M.G., 2003. Discontinuous Galerkin and the Crouzeix-Raviart element: Application to elasticity. *Mathematical Modelling and Numerical Analysis* 37, 63–72.

Henao, D., Mora-Corral, C., Xu, X., 2016. A numerical study of void coalescence and fracture in nonlinear elasticity. *Computer Methods in Applied Mechanics and Engineering* 303, 163–184.

Hesch, C., Weinberg, K., 2014. Thermodynamically consistent algorithms for a finite-deformation phase-field approach to fracture. *International Journal for Numerical Methods in Engineering* 99, 906–924.

Kumar, A., Aranda-Iglesias, D., Lopez-Pamies, O., 2017. Some remarks on the effects of inertia and viscous dissipation in the onset of cavitation in rubber. *Journal of Elasticity* 126, 201–213.

Lake, G.J., Thomas, A.G., 1967. The strength of highly elastic materials. *Proceedings of the Royal Society of London A* 300, 108–119.

Lefèvre, V., Ravi-Chandar, K., Lopez-Pamies, O., 2015. Cavitation in rubber: an elastic instability or a fracture phenomenon?. *International Journal of Fracture* 192, 1–23.

Lopez-Pamies, O., 2010. A new I_1-based hyperelastic model for rubber elastic materials. *Comptes Rendus Mecanique* 338, 3–11.

Maurini, C., Bourdin, B., Gauthier, G., Lazarus, V., 2013. Crack patterns obtained by unidirectional drying of a colloidal suspension in a capillary tube: experiments and numerical simulations using a two-dimensional variational approach. *Int. J. Fract.* 184, 75–91.

Mesgarnejad, A., Bourdin, B., Khonsari, M.M., 2015. Validation simulations for the variational approach to fracture. *Computer Methods in Applied Mechanics and Engineering* 290, 420–437.

Miehe, C., Schänzel, L.M., 2014. Phase field modeling of fracture in rubbery polymers. Part I: Finite elasticity coupled with brittle failure. *Journal of the Mechanics and Physics of Solids* 65, 93–113.

Mielke, A., 2003. Energetic formulation of multiplicative elasto-plasticity using dissipation distances. *Continuum Mechanics and Thermodynamics* 15, 351–382.

Mielke, A., Theil, F., 2004. On rate-independent hysteresis models. *Nonlinear Differential Equations and Applications* 11, 151–189.

Mullins, L., 1959. Rupture of rubber. IX. Role of hysteresis in the tearing of rubber. *Transactions of the Institution of the Rubber Industry* 35, 213–222.

Negri, M., 1999. The anisotropy introduced by the mesh in the finite element approximation of the Mumford-Shah functional. *Numerical Functional Analysis and Optimization* 20, 957–982.

Negri, M., 2003. A finite element approximation of the Griffith's model in fracture mechanics. *Numerische Mathematik* 95, 653–687.

Neuberger, J.W., 2010. *Sobolev Gradients and Differential Equations*. Springer, Heidelberg.

Pham, K., Amor, H., Marigo, J.J., Maurini, C., 2011. Gradient damage models and their use to approximate brittle fracture. *International Journal of Damage Mechanics* 20, 618–652.

Poulain, X., Lefèvre, V., Lopez-Pamies, O., Ravi-Chandar, K., 2017. Damage in elastomers: Nucleation and growth of cavities, micro-cracks, and macro-cracks. *International Journal of Fracture* 205, 1–21.

Ravi-Chandar, K., 2016. Private communication.

Rivlin, R.S., Thomas, A.G., 1953. Rupture of rubber. Part I. Characteristic energy for tearing. *Journal of Polymer Science* 10, 291–318.

Rui, H., Zhang, R., 2009. A unified stabilized mixed finite element method for coupling Stokes and Darcy flows. *Computer Methods in Applied Mechanics and Engineering* 198, 2692–2699.

Sicsic, P., Marigo, J.-J., 2013. From gradient damage laws to Griffith's theory of crack propagation. *Journal of Elasticity* 113, 55–74.

Truskinovsky, L., 1996. Fracture as a phase transition. In *Contemporary Research in the Mechanics and Mathematics of Materials*, Eds. R.C. Batra and M.F. Beatty, pp. 322–332, CIMNE, Barcelona.

Winkler B.J., 2001. *Traglastuntersuchungen von unbewehrten und bewehrten Betonstrukturen auf der Grundlage eines objektiven Werkstoffgesetzes fur Beton [Load tests of unreinforced and reinforced concrete structures on the basis of an objective material law for concrete]* (PhD thesis). Innsbruck University Press.

Xu, X., Henao, D., 2011. An efficient numerical method for cavitation in nonlinear elasticity. *Mathematical Models and Methods in Applied Sciences* 21, 1733–1760.